Composites Part B 328 (2027) 114209

Contents lists available at ScienceDirect

Composites Part B

journal homepage: www.elsevier.com/locate/compositesb

Power ultrasound enhancement of diatomite-containing cement-based composites: multi-scale composite engineering of the interfacial transition zone and micromechanical homogenization

Paweł Lisowski *, Daria Jóźwiak-Niedźwiedzka, Kamil Bochenek, Michał A. Glinicki **

Institute of Fundamental Technological Research Polish Academy of Sciences, Pawinskiego 5b, Warsaw, 02-106, Poland

ARTICLE INFO

Keywords:
Particulate composite
Interfacial transition zone
Micromechanical homogenization
Power ultrasound treatment
Diatomite powder
Nearest-surface distribution
ITZ percolation

ABSTRACT

This study investigates the multi-scale composite engineering of diatomite powder (DP)-modified micro-concrete subjected to power ultrasound (PUS) treatment. The main findings demonstrate that the combined DP + PUS treatment significantly improves macroscopic performance, increasing 28-day compressive strength by 60% in diabase (DI, 43.6 MPa) and 55% in limestone (LS, 44.1 MPa) systems, despite a 20% cement replacement. Microstructurally, DP selectively eliminates large macropore defects (>1000 nm) predominantly localized at the aggregate-paste boundary, as independently confirmed by fluorescence microscopy and SEM, reducing their volume fraction from 5.22% to 0.26% (DI) and from 3.43% to 0.56% (LS). In limestone systems, PUS further decreases the interfacial transition zone (ITZ) width by ~62% (from ~150 μm to 57.4 μm) and increases cement matrix hardness by 27.4%. Lu-Torquato spatial modelling confirms that this ITZ narrowing reduces the 3D weak-phase volume fraction from 3.0% to 1.1%, effectively disrupting the percolated interfacial network. Mori–Tanaka micromechanical homogenization further predicted a corresponding 7.5% increase in composite elastic modulus (32.2 → 34.6 GPa), confirming the mathematical coherence between microstructural refinement and macroscopic stiffness gains. These results provide direct experimental evidence that macroscopic strength is primarily governed by the selective elimination of large macropores and ITZ refinement rather than a mere reduction in total bulk porosity.

1. Introduction

Cement-based micro-concrete constitutes a two-phase particulate composite system in which mineralogically distinct aggregate inclusions are embedded within a hydrating cementitious matrix. The mechanical response and failure trajectory of this composite are governed not solely by the bulk properties of either constituent phase, but critically by the characteristics of the matrix–inclusion interface, the interfacial transition zone (ITZ) [1–6]. In particulate composites, this interfacial region represents the weakest link in the composite architecture: its elevated porosity, reduced stiffness, and propensity for geometric percolation between adjacent inclusions collectively dictate quasi-brittle failure initiation and macroscopic stress-strain nonlinearity [1–6]. Elevated total porosity is frequently cited as the primary indicator of ITZ weakness; however, emerging evidence suggests that large macrodefects exceeding 1000 nm may govern mechanical performance more decisively than overall void volume alone, a distinction with direct implications for composite engineering and mix design optimisation [5, 6].

Engineering the matrix–inclusion interface in particulate composites can be achieved through microstructural modification strategies that address particle packing efficiency, pozzolanic densification, and interfacial bonding mechanisms [1–6]. These strategies are broadly classified into: (i) pre-treatment methods involving chemical or polymer modification of inclusion surfaces before composite preparation, and (ii) partial replacement of the matrix binder with supplementary cementitious materials (SCMs), which participate in particle packing densification, latent hydraulic reactions, and pozzolanic reactions to progressively densify the interfacial zone [1–7]. The effectiveness of such interventions is inherently coupled to the physico-chemical compatibility between the matrix and inclusion phases, a relationship that this study explicitly exploits by comparing reactive calcareous

* Corresponding author.
** Corresponding author.
E-mail addresses: plisowsk@ippt.pan.pl (P. Lisowski), mglinic@ippt.pan.pl (M.A. Glinicki).

https://doi.org/10.1016/j.compositesb.2026.114209
Received 9 June 2026; Received in revised form 7 September 2026; Accepted 8 September 2026
Available online 8 September 2026

(limestone, LS) and chemically inert igneous (diabase, DI) inclusions within an otherwise identical composite system. Elevated ITZ porosity compromises both the mechanical performance and long-term durability of the composite [8].

ITZ microstructure depends on parameters such as aggregate roughness, particle size, and the w/c ratio [9–11]. Porosity gradients are steeper near smooth surfaces than near rough interfaces [10,11]. The influence of SCMs on ITZ microstructure is multifaceted and remains inadequately characterized, particularly regarding quantitative assessments, owing to the non-discrete nature of the ITZ and the need for specialized characterization methodologies. These complexities are amplified in ternary blended systems [12].

The characteristics of the ITZ are profoundly influenced by aggregate mineralogy. Limestone, characterized by a Mohs hardness of 2.7-3.0 and a relatively smooth surface, actively engages in carbonate-silicate reactions with the hydrating cement [13,14]. Conversely, the significantly harder diabase (6.0-6.5 Mohs) relies entirely on its distinctly rough surface for mechanical adhesion, lacking the direct chemical compatibility observed in calcareous aggregates [15,16]. Recent investigations have revealed that the indentation modulus of the ITZ around limestone aggregates (LS) exceeds that of other aggregate types, whereas the ITZ thickness around LS aggregates is comparatively reduced [16–19]. This is attributed to the enhanced chemical compatibility, improved cement particle packing, and high surface free energy of alkaline calcareous substrates, which promote the oriented nucleation and growth of hydration products directly at the calcareous interface [19].

The physical obstruction caused by coarse aggregates disrupts the dense arrangement of cement particles, thereby initiating a microstructural gradient known as the wall effect. This inefficient packing is often worsened by the localized accumulation of a distinct water film beneath the aggregate surfaces [2,20–23]. This proximity leads to the overlapping (percolation) of neighbouring ITZ regions, which fundamentally alters the micro- and meso-scale pore structure of the composite [24]. Even in mature pastes, the ITZ maintains significantly higher porosity [25]. In standard concrete mixtures, the reduced "spacing factor" between aggregates leads to ITZ percolation, fundamentally altering mass transport and stress-strain behaviour of the composite [26,27]. Rough aggregate surfaces introduce a secondary disruption of particle packing, analogous to the wall effect, yielding ITZ regions with greater apparent thickness and porosity [9,11,28]. Accurate ITZ characterisation requires careful correction of stereological errors inherent in 2D sectioning [29], and advanced depth-sensing microindentation to map local elastic modulus (EM) gradients [17,30,31] - the local parameters that ultimately govern quasi-brittle failure and nonlinear stress-strain behaviour at the macroscale. Recent micromechanical studies based on Griffith's microcracking theory further demonstrate that ITZ thickness and micro-properties, which are heavily influenced by the coarse aggregate size and the incorporation of mineral powders, act as critical initial flaws governing this quasi-brittle failure [32,33].

Advanced composite processing techniques have been developed to engineer the matrix–inclusion interface beyond the limits achievable through conventional mixing. This aligns with recent advancements in sustainable composite engineering, where the strategic utilization of low-grade minerals or industrial by-products, such as coal gasification slag, is increasingly employed to produce eco-friendly, high-performance composites with enhanced matrix density and optimized working properties [34]. Among these, power ultrasound treatment (PUS) has emerged as a high-potential method for improving the microstructure of fresh particulate composite systems [35,36]. When applied during matrix preparation, PUS disrupts binder particle clusters, reduces agglomeration, and enhances particle packing efficiency at the inclusion surface through acoustic energy [35]. Recent advances in sonochemistry have demonstrated that PUS functions as an effective acoustic defoaming technology for composite matrices: oscillating bubbles driven by secondary Bjerknes forces cause dispersed air pockets to merge and escape, systematically purging the matrix of internal voids that would otherwise act as stress concentration sites at the matrix–inclusion interface [37]. Furthermore, the application of acoustic energy bypasses standard thermal activation thresholds, triggering early formation of calcium silicate hydrate and portlandite nucleation seeds, thereby accelerating the dormant hydration phase and producing an earlier-consolidating matrix phase [38]. Crucially, the acoustic defoaming mechanism preferentially targets large macropore defects (>1000 nm), the primary Griffith-type stress concentrators within the ITZ, rather than uniformly reducing total porosity, implying that PUS-induced composite strength gains are more closely related to critical macropore elimination than to bulk void reduction alone [37]. The efficacy of PUS on ITZ properties varies with inclusion mineralogy, reflecting the distinct surface free energies and chemical compatibility of different aggregate types with the hydrating matrix phase [28,39–42]. For LS aggregates, which inherently form a relatively dense ITZ owing to their favorable chemical compatibility with cement, PUS may further enhance the interface by promoting superior particle packing and reducing initial porosity gradients [28,39–42]. For diabase aggregates (DI), PUS primarily acts through physical consolidation and improved dispersion, helping fill the irregular surface features characteristic of igneous rocks and creating a more continuous transition between the aggregate and the paste. However, the absence of chemical bonding mechanisms between the inert silicate surface and the CM (cement matrix) constrains the magnitude of interfacial improvement relative to that achievable in LS systems [28,39–42].

Diatomite powder (DP) is a siliceous sedimentary rock containing abundant amorphous silica particles derived from fossilized algal skeletons and shells [43]. DP serves as an effective SCM due to its distinct chemical and physical properties, such as a small particle size that enables interstitial space filling between cement particles and pozzolanic reactivity (PR) attributable to its high silica content [43]. DP incorporation alters the hydration process and modifies the distribution of pore sizes in cement-based materials. Due to both hydration reactions and the intrinsically porous nature of the DP surfaces, Sun et al. [44] found that increasing the DP dosage improved the material porosity (as evaluated by MIP). Excessive DP dosage led to progressive coarsening of the pore structure. Akhtar et al. [45] reported that sintering of DP eliminates fine porosity, with compressive strength (f_c) of sintered monoliths increasing with temperature up to ~1000 °C.

PUS has been employed to influence DP's physical properties. Zhang et al. [46] demonstrated that 8 min of sonication increased DP porosity, decreased its density, and elevated surface area. Lorwanishpaisarn et al. [47] observed substantial increases in BET surface area with sonication treatment duration up to 60 min. These microstructural improvements are driven by the cyclical creation and collapse of vibratory bubbles during acoustic wave propagation. Dynamic pressure changes strip away blockages from the DP surface, clearing obstructed channels while preserving the particle core integrity [46]. The modified Chapelle test, conducted by Lisowski et al. [43], revealed that DP sonication increased $Ca(OH)_2$ intake by up to 1984 mg/g. Building upon previous findings focused primarily on bulk paste properties [36,43], the current research specifically examines how ultrasonic activation of DP influences the localized microstructural features of the ITZ in micro-concrete. Sonication resulted in the best-performing DP + cement paste (CP) with significantly higher early f_c and f_{fl} and shorter setting times. Therefore, the novelty of this study lies not in the mere application of PUS but in its strategic use as a tool for advanced multi-scale composite engineering. While prior works were strictly limited to single-phase binder reactivity, this research addresses the highly complex, localized microstructural modifications within two-phase particulate systems. We would also like to clarify that, while the broader literature on PUS applications in cementitious systems is indeed substantial, no prior study has jointly investigated PUS-activated SCM performance across two mineralogically contrasting aggregate types (chemically reactive limestone versus chemically inert diabase) within the same experimental framework. This

comparative design is not incidental: it is precisely what allows us to isolate the relative contributions of chemical bonding versus purely physical consolidation to ITZ engineering, a distinction that cannot be established from single-aggregate or single-phase studies. Furthermore, the specific methodological combination employed here, quantitative fluorescence-based ITZ mapping, depth-sensing microindentation, and analytical upscaling via the Lu–Torquato and Mori–Tanaka frameworks, has, to our knowledge, not been previously applied to a PUS-treated, SCM-modified particulate composite system. This integrated approach is what enables us to mathematically connect nanoscale interfacial defect healing to macroscopic strength and stiffness gains, going substantially beyond the scope of prior PUS studies focused on bulk paste reactivity alone. This study presents several novel contributions to the field of cement-based materials and ITZ enhancement.

1. Systematic investigation of combined DP + PUS treatment across chemically distinct aggregate types - No prior study has jointly examined the effects of PUS-activated DP on ITZ microstructure for both reactive (LS) and inert (DI) aggregates. This work establishes aggregate mineralogy as a critical parameter in PUS optimisation and provides direct experimental evidence that macroscopic strength is governed by selective elimination of accessible large macropore defects (>1000 nm) rather than total porosity reduction alone.
2. Integration of R^3 reactivity test methodology with PUS treatment optimisation - This work pioneers the application of isothermal calorimetry using the R^3 method to quantitatively assess and optimise PUS treatment parameters for SCMs, establishing the optimal treatment threshold through systematic heat-release measurements.
3. Multi-scale characterisation combining fluorescence microscopy, nanoindentation, SEM, and MIP - The study employs convergent advanced characterisation techniques, including a fluorescence-based image analysis method for quantitative determination of ITZ thickness.
4. Demonstration of a waste material valorisation pathway - This research establishes a practical method for upgrading locally available, low-grade DP (low SiO_2) into a highly reactive SCM, validating R^3 calorimetry as a rapid screening tool for SCM processing optimisation.

The primary objective of this study is to establish how the mineralogical character of the inclusion phase, specifically the contrast between chemically reactive calcareous (LS) and chemically inert igneous (DI) inclusions, governs the magnitude of ITZ engineering achievable through PUS processing of a DP-modified cementitious matrix composite. A secondary objective is to determine whether macroscopic composite strength gains are more closely correlated with the selective elimination of large macropore defects (>1000 nm), identified as Griffith-type stress concentrators predominantly located at the matrix–inclusion boundary, than with overall porosity reduction, a distinction that challenges conventional porosity–strength relationships in particulate composite design. The R^3 isothermal calorimetry methodology was employed to identify the optimal PUS treatment duration, balancing acoustic energy input against SCM reactivity enhancement for potential industrial-scale composite fabrication. To this end, a convergent multi-scale experimental framework was employed, integrating fluorescence microscopy with digital image analysis, depth-sensing microindentation, scanning electron microscopy, and mercury intrusion porosimetry, with results analytically upscaled via Lu–Torquato spatial modelling and Mori–Tanaka micromechanical homogenization. Ultimately, the practical and environmental value of this research lies in establishing an energy-efficient, industrially viable pathway for the upcycling of widely available, low-grade natural minerals into high-performance sustainable composites, completely circumventing the need for carbon- and energy-intensive thermal calcination.

2. Experimental program

2.1. Materials and specimens

The micro-concrete specimens investigated in this study are modelled as two-phase particulate composites, with crushed aggregate (LS or DI) serving as the inclusion phase and Portland cement paste partially substituted with diatomite powder constituting the continuous matrix phase; this composite architecture provides a controlled experimental platform for isolating the effects of inclusion mineralogy on ITZ engineering. The selection of raw materials was as follows.

- CEM I 42.5 R in accordance with EN 197-1,
- DP from Poland's Podkarpackie Voivodeship in Jawornik Ruski,
- Quartz Sand CEN Standard in accordance with EN 196-1,
- Tap water,
- DI and LS crushed aggregates.

Table 1 shows the chemical composition of DP and cement. DP has a SiO_2 content of about 70% and an LOI of about 9%, which is considered a low-grade DP [48–50]. This relatively high LOI value is characteristic of natural, minimally processed diatomite and is primarily attributed to the thermal decomposition of organic matter, dehydroxylation of clay minerals, decarbonation of carbonate impurities, and the dehydration of amorphous silica (opal-A) [43,48–50]. This is consistent with literature-reported LOI values for raw and low-grade diatomites, which range from approximately 0.1% to 36.6% depending on deposit and processing degree [43]. The study's aggregate physical properties (Table 2) are typical for the type of rock considered, which is consistent with the literature [28,39–42].

The reference mortar mixture (REF) was prepared at a w/c ratio of 0.50, using 450 g of cement and 1350g of quartz sand. The micro-concrete (MC) mix design is shown in Table 3. With respect to a typical, well-proportioned concrete mix, this is a model concrete with increased paste content and reduced sand content, assumed to enhance the effects of aggregate-paste contact zones.

DP (125–250 μm) was used as a constituent of MC to substitute 20 wt % of Portland cement, yielding a water-to-binder ratio (w/b) = 0.50 (w = 225 g, total binder = cement 360 g + DP 90 g = 450 g). This replacement level was selected based on preliminary trials and literature recommendations: higher DP dosages cause excessive pore coarsening and reduce workability. In comparison, lower dosages provide insufficient reactive silica for effective pozzolanic ITZ densification. Although the as-sieved DP fraction used in all micro-concrete mixtures was 125-250 μm, PUS induces progressive sonofragmentation of these particles during paste preparation. Laser granulometric analysis of the DP fraction (125-250 μm) subjected to 10 min of PUS revealed a dramatic reduction in particle size: the D_{50} decreased from 110.0 μm to 9.7 μm and the D_{90} from 207.0 μm to 47.5 μm, with the sub-63 μm mass fraction increasing by 524% relative to the untreated material [40]. Consequently, the effective particle size of DP at the moment of aggregate–paste contact is well below the measured ITZ width (30-150 μm), confirming that sonofragmented DP particles are geometrically capable of filling and densifying the interfacial zone. This particle-size reduction is the primary physical mechanism enabling an initially coarse, low-grade DP fraction to function as an effective ITZ modifier.

Sonicated mixtures were prepared in two steps: first, the paste components were sonicated, and then, in accordance with PN-EN 196-1, the fresh paste was mixed with DI and LS aggregates in a standard mortar mixer. To apply the PUS, the cementitious mixtures were processed in a glass cooling-jacket reactor coupled with a 700 W, 20 kHz QSonica Q700 device. Thermal control during the procedure was maintained using a pulsed operation cycle that alternated between 5 s of active ultrasonic irradiation (sonication) and 5 s of rest, following protocols established in prior work [36,43].

During the first 24 h of curing at laboratory conditions of 20–23 °C

Table 1
DP and cement's chemical composition.

Material	Chemical composition [%]											
	CaO	SiO_2	Fe_2O_3	Al_2O_3	SO_3	MgO	TiO_2	Na_2O	K_2O	Mn_2O_3	P_2O_5	LOI
CEM I 42.5 R	61.74	19.54	2.83	4.75	3.14	3.21	0.23	0.16	0.90	0.17	0.12	3.08
DP	0.60	69.68	4.51	10.99	0.13	1.17	0.47	0.52	2.32	0.18	0.12	9.27

Table 2
Physical properties of LS and DI aggregate.

Property	LS	DI	Ref
Apparent particle density ($g{\cdot}cm^{-3}$)	2.71 ± 0.01	2.80 ± 0.03	This study Particle density and water absorption calculations in accordance with PN-EN 1097-6
Particle density in an oven-dried environment ($g{\cdot}cm^{-3}$)	2.68 ± 0.01	2.77 ± 0.03	
Surface-dried and saturated particle density ($g{\cdot}cm^{-3}$)	2.69 ± 0.01	2.78 ± 0.03	
Water absorption WA_{24} (%)	0.36 ± 0.03	0.38 ± 0.02	
Apparent relative density ($g{\cdot}cm^{-3}$)	2.67 – 2.88	2.74 – 2.97	28, 39-42
Crushed value (%)	10.4 – 20.8	6.0 – 11.4	28, 39, 41-42
Water absorption (%)	0.25 – 1.49	0.42 – 1.48	28, 39-42
Angularity	31.8	35.4	28, 39
Los-Angeles Abrasion (%)	15.59	5.33	41
Roundness Index	0.72	0.78	41
Flakiness Index (%)	9	4	41
Hardness (Mohs)	2.7~3.0	6.0~6.5	41
Sand Equivalent (%)	76.12	79.85	41

Table 3
MC mixture proportions.

Mixture designation *)	Cement [g]	DP [g]	H_2O [g]	Aggregates [g]
MC_DI MC_DI_10 min. PUS	450	-	225	900.4 (#4-8 mm) + 449.6 (#8-12.5 mm) - DI
MC_LS MC_LS_10 min. PUS				900.4 (#4-8 mm) + 449.6 (#8-12.5 mm) - LS
MC_DI + DP MC_DI + DP_10 min. PUS	360	90		900.4 (#4-8 mm) + 449.6 (#8-12.5 mm) - DI
MC_LS + DP MC_LS + DP_10 min. PUS				900.4 (#4-8 mm) + 449.6 (#8-12.5 mm) - LS

and 60–70% RH, the reference mortar mixture and MC mixtures were cast into prismatic moulds (40 x 40 × 160 mm), compacted on a vibrating table, and tightly covered. The specimens were cured in water at 20-23 °C for 2, 7, or 28 d after demolding before testing.

2.2. Test methods

The R^3 heat-release test [51–55] was employed to evaluate the sonication-induced reactivity of DP. This technique simultaneously evaluates combined pozzolanic and latent hydraulic activity, effectively isolating the thermal contribution of DP from standard clinker hydration. A multichannel isothermal calorimeter (Calmetrix I-Cal 2000 HPC) was used to measure heat release over seven days at 40 °C, following the manufacturer's instructions to use a Mylar bag to prevent moisture loss. Unlike traditional methods such as the Strength Activity Index (SAI) or the Chapelle test, the R^3 protocol (standardized as EN 196-12) eliminates the confounding variables of clinker hydration variability and physical filler effects [51,56]. This isolation makes it highly appropriate and uniquely suited for accurately tracking the intrinsic activation efficiency of the PUS treatment on the diatomite powder.

The robustness and inter-laboratory reproducibility of this protocol have been extensively validated through the RILEM TC 267-TRM round-robin testing programme, which confirmed its reliability across a wide range of conventional and emerging pozzolanic materials [51,57]. Nevertheless, as the R^3 test is conducted under simplified, filler-free conditions at elevated temperature, its results are used here strictly as a relative indicator of PUS-induced activation efficiency rather than as a direct quantitative predictor of in-situ concrete hydration kinetics, consistent with its intended scope of application [58].

The flexural (f_{fl}) and compressive (f_c) strengths of mortar and MC were examined on 40 × 40 × 160 mm specimens using an Automax Controls Pro (Italy) testing machine, following 2, 7, and 28 d of hardening. A minimum of three replicate specimens (n = 3) were tested per mixture per age; results are reported as mean ± standard deviation (SD). The remaining specimen halves underwent f_c testing following f_{fl} testing.

The hardened specimens (40 × 40 × 160 mm) were cut into smaller pieces (10 × 25 × 40 mm) before microindentation testing. Depth-sensing indentation tests were conducted using a Lloyd EZ 50 testing apparatus with a load cell (capacity of 50 N at an accuracy better than 0.5%) and an LVDT transducer to measure the displacement of the Vickers indenter with an accuracy of 0.1 μm [59,60]. Fifteen measurements per zone (ITZ, CM, aggregate) were averaged; indentation positions were recorded to within ± 5 μm of the aggregate boundary as identified in the corresponding optical image. These local-phase properties were subsequently used as fundamental input parameters for micromechanical homogenization.

For SEM analysis, specimens cured for 7 d were cut, polished with diamond pastes, vacuum-impregnated with low-viscosity epoxy, and carbon-coated; examined in backscattered electron (BSE) mode using a Zeiss Crossbeam 350 microscope.

Thin sections of concrete prisms were used to evaluate the microstructure in accordance with ASTM C856 [61]. For this investigation, low-viscosity fluorescent epoxy was vacuum-impregnated into 40 × 50 mm concrete blocks and thin sections were prepared in accordance with [62,63]. Using low-viscosity glue and a yellow fluorescent dye, the blocks were vacuum-impregnated. The thin sections, 20 ± 2 μm thick, were prepared using a Pelcon thin-section machine. An Olympus BX51 optical polarising microscope, coupled with a digital camera, was used for thin-section analysis [64,65]. Individual 2.2 × 1.65 mm^2 high-resolution photos (1 px = 0.86 μm) were taken from a thin section and stitched together to create a full thin-section image using Image Composite Editor software (lossless compression, original resolution retained). In cross-polarised light and ultraviolet light, certain binarization procedures and morphological filters (dilatation, erosion) were employed to distinguish various concrete phases in thin-section images. The accurately determined 2D apparent ITZ boundaries were then explicitly utilized to calculate the true 3D spatial volume fraction (V_{ITZ}).

The pore size distribution of hardened concrete specimens produced with or without sonication was examined using mercury intrusion porosimetry (MIP). Following a conventional 28 d hardening period, the small cores were cut and dried at 40 °C until constant mass was achieved, then measured for MIP. The specimen dimensions (ø = 9 mm, h = 25 mm) were selected to fit the measurement cell of the Poremaster 60 mercury porosimeter from Quantachrome. The porosimeter was operating at its maximum pressure of 414 MPa. The Washburn

relationship defined the minimum detectable pore diameter at about 3 nm, and total porosity was calculated as the ratio of intruded mercury volume to bulk specimen volume [66]. It should be acknowledged that MIP is subject to the ink-bottle effect, whereby large pores accessible only through narrow throats are recorded at the throat diameter rather than the true cavity diameter. This may systematically overestimate the proportion of small pores (10-100 nm) and underestimate the proportion of large macropores (>1000 nm). Interpretation of pore-size categories should be made with this limitation in mind, and therefore, the dramatic reduction in macropores reported herein must be interpreted as a highly significant relative trend rather than an absolute 3D volumetric measure.

2.3. Analytical upscaling and micromechanical modelling

To validate the relationship between local microstructural enhancements and macroscopic strength gains, analytical modelling was integrated with the experimental framework. The nearest-surface distribution function (the Lu-Torquato model) [67] was employed to determine the ITZ's actual 3D volume fraction (V_{ITZ}) from 2D spatial boundaries measured via fluorescence microscopy. Subsequently, a Mori-Tanaka micromechanical homogenization scheme was applied, treating the bulk CP as the reference matrix and the aggregate particles as spherical inclusions. The ITZ effect is accounted for indirectly through the measured change in paste EM adjacent to the interface. By utilizing the specific elastic properties of the individual phases (aggregate, ITZ, and bulk paste) obtained from microindentation mapping, this continuum micromechanics model theoretically predicts the composite's macroscopic EM, thereby mathematically connecting nanoscale defect healing to global structural performance.

3. Results

3.1. DP reactivity

Fig. 1 presents isothermal calorimetry data at 40 °C over 168 h. Untreated DP displayed a primary peak at approximately 12 h, reaching ~3.0 mW/g, followed by a gradual decline to ~1.5 mW/g by 72 h. DP subjected to 5 min PUS treatment showed a peak of ~3.1 mW/g.

The DP_10 min. PUS treatment produced a peak of approximately 3.2 mW/g, with sustained heat release rates elevated throughout the 24-168 h period compared to untreated specimens. The DP_15 min. PUS specimen exhibited the highest peak intensity (~3.3 mW/g) and maximum sustained heat release rates. Cumulative heat release values at

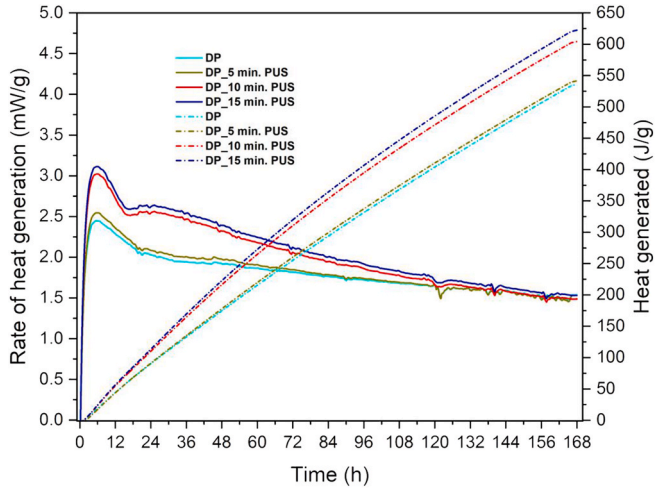

Fig. 1. DP's reactivity under the sonication treatment assessed by isothermal calorimetry.

168 h are presented in Table 4. Values ranged from 535.8 J/g (untreated) to 541.6, 604.3, and 622.4 J/g for 5, 10, and 15 min. PUS treatments, respectively.

The 10 min PUS treatment delivering 12.8% reactivity enhancement versus 15-min. treatment yielding only 16.2% (3.0% marginal gain for 50% additional energy input) clearly identifies the 10 min duration as the optimal processing parameter. It should be noted that the R^3 test conditions (40 °C, $Ca(OH)_2$ + $CaCO_3$ + potassium solution, absence of aggregates) differ markedly from the concrete mixing environment. The reactivity ranking established by R^3 calorimetry is used here as a relative indicator of enhanced potential reactivity, and its direct proportional relationship with the complex, room-temperature hydration kinetics of the multi-phase concrete composite should be treated as a qualitative correlation rather than a direct quantitative prediction. The data reveal a non-linear relationship between PUS treatment duration and reactivity enhancement. Gains were minimal at 5 min (+1.1%), substantial at 10 min (+12.8%), and diminished at 15 min (+3.0% relative to 10 min), suggesting saturation of activation mechanisms beyond the 10 min threshold, potentially due to re-agglomeration or excessive particle fragmentation. The 12.8% increase in cumulative heat release for DP_10 min PUS directly correlates with the mechanical strength improvements observed in Figs. 3 and 4, where 10 min PUS treatment combined with DP achieved optimal f_{fl} and f_c.

3.2. f_{fl} and f_c

The f_{fl} and f_c development of reference mortar is presented in Fig. 2. The f_c increases with time (23.6 MPa at 2 d, 36.8 MPa at 7 d, and 47.3 MPa at 28 d) and is consistent with the expected performance of a CEM I 42.5 R.

A similar relative increase in f_{fl} was observed, from 5.7 MPa at 2 d to 9.3 MPa at 28 d. Figs. 3 and 4 illustrate the composite specimens' mechanical performance. Both aggregate types showed similar baseline flexural strength at 28 d (~4.4–4.5 MPa), with a modest difference at 2 d (MC_DI: 2.8 MPa, MC_LS: 2.9 MPa).

PUS alone raised 28 d f_{fl} to 5.5 MPa (DI) and 5.7 MPa (LS), and combined DP + PUS further increased it to 6.6 and 7.3 MPa, respectively - a 50-62% improvement over controls. Baseline compressive strengths were 27.3 MPa (MC_DI) and 28.4 MPa (MC_LS) at 28 d (Fig. 4). DP addition alone produced a more modest gain in the LS system than in DI, likely reflecting the already relatively dense LS-paste interface and limited early-age pozzolanic contribution at w/b = 0.50. PUS treatment alone yielded 40.6 MPa (DI) and 42.1 MPa (LS) at 28 d. The combined DP + PUS treatment achieved the highest gains: 43.6 MPa (DI) and 44.1 MPa (LS), representing 60% and 55% improvements over the unmodified controls, respectively.

3.3. Pore size distribution

Fig. 5 and Table 5 illustrate the influence of aggregate type, DP addition, and PUS treatment on pore size distribution determined by MIP. A significant difference in intrinsic rock porosity was measured: 2.52% for DI and 7.02% for LS, which underlies the consistently higher baseline total porosity in all LS-based mixtures (+2.3 pp versus DI equivalents). Pore sizes are categorised as small (10-100 nm), intermediate (100-1000 nm), and large (>1000 nm).

PUS alone substantially reduced small-pore content in both systems

Table 4
Cumulative heat release according to EN 196-12:2024 (method A) [54].

PUS treatment	Heat release at 168 h (J/g DP)
DP (none)	535.8
DP_5 min. PUS	541.6
DP_10 min. PUS	604.3
DP_15 min. PUS	622.4

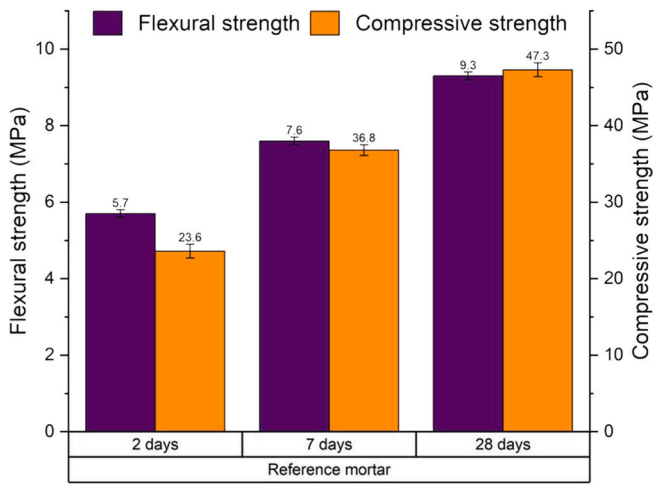

Fig. 2. f_{fl} and f_c of reference mortar.

(DI: 6.67% → 1.59%; LS: 10.94% → 6.26%), with more limited and occasionally complex effects on intermediate and large pores. In the DI system, this total porosity reduction of >6 pp by PUS alone (from 12.86% to 6.16%) corresponded to flexural and compressive strength gains of ~25% and ~49%, respectively, providing direct quantitative evidence of the pore structure–strength relationship for the PUS-alone treatment.

Within the tested systems, the dominant benefit of DP addition was the selective elimination of accessible large macropore defects (>1000 nm), which dropped from 5.22% (MC_DI) to 0.26% (MC_DI + DP) in the DI system, and from 3.43% (MC_LS) to 0.56% (MC_LS + DP) in the LS system. While MIP evaluates the continuous pore system of the entire bulk composite and cannot independently resolve the spatial location of these pores [68,69], our correlative fluorescence microscopy and SEM observations (Sections 3.4 and 3.6) provide independent visual evidence that such large void spaces are predominantly localized at the aggregate-paste boundary. Therefore, the substantial elimination of >1000 nm voids measured by MIP can be confidently linked to the densification of the ITZ.

The subsequent application of PUS primarily contributed to densifying smaller capillary pores and to the overall hardening of the matrix, resulting in final macropore volumes of 0.36% (DI) and 0.42% (LS). Effects on intermediate pores remained modest (ranging from −0.14 pp to +0.55 pp), while small-pore content increased by 1.94 pp (LS: 7.11% → 9.05%) and 3.37 pp (DI: 1.71% → 5.08%) within DP-containing systems, reflecting a synergistic combination of factors: the generation of additional C-S-H gel porosity via pozzolanic reaction, the progressive refinement of larger capillary pores, and the physical unclogging of intrinsic DP pores by acoustic cavitation [46,47]. Notably, the best-performing mixture (MC_LS + DP_10 min. PUS, f_c = 44.1 MPa) displayed higher total porosity (11.24%) than its unsonicated counterpart (MC_LS + DP, 8.89%), yet achieved superior mechanical performance - a 'porosity paradox' discussed in Section 4.2. In the LS system, DP alone reduced total porosity by > 6 pp, but subsequent PUS raised it by ~2.4 pp, suggesting complex interactions between calcareous surface reactions and acoustic activation that warrant further study.

Notably, the same phenomenon is observed in the DI system: MC_DI + DP_10 min. PUS exhibited total porosity of 6.01%, substantially higher than its unsonicated counterpart MC_DI + DP (2.39%), yet achieved markedly superior compressive strength (43.6 vs. 30.5 MPa). This confirms that the porosity paradox is not aggregate-specific but a systemic consequence of the selective macropore-to-gel-pore redistribution induced by the DP + PUS combination.

3.4. ITZ imaging

Fluorescence intensity in epoxy-impregnated thin sections is proportional to local capillary porosity, enabling quantitative ITZ mapping [23,70,71]. Perpendicular measurement trajectories were projected from aggregate boundaries into the CM following established stereological protocols [7,24,29], with ITZ thickness defined as the distance at which intensity stabilises to bulk-paste levels [26,67,72]. Only boundaries perpendicular to the cutting plane were selected to eliminate stereological overestimation [29].

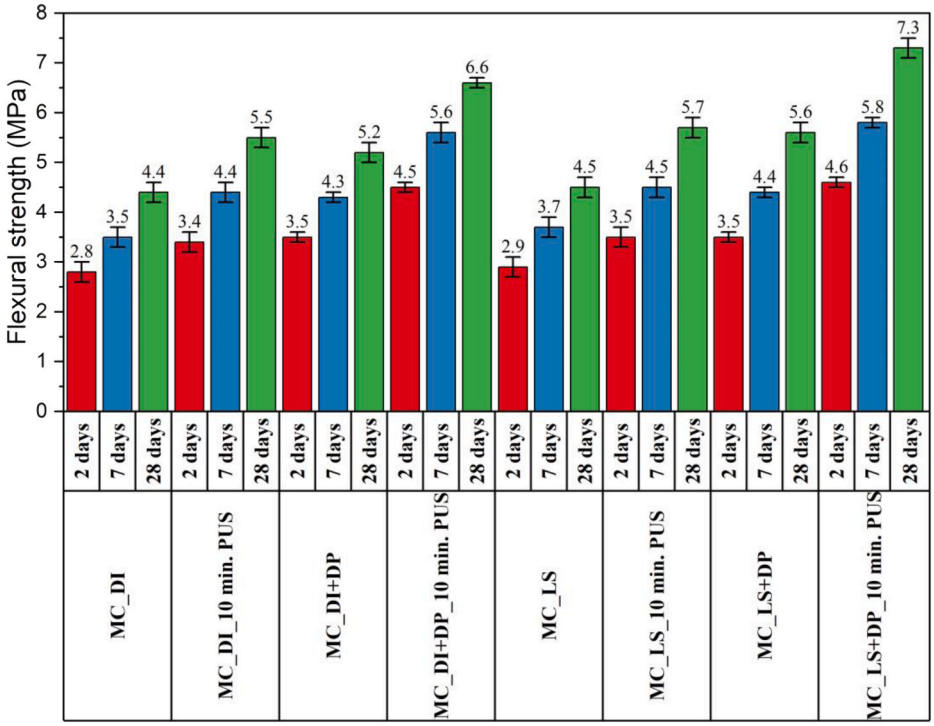

Fig. 3. f_{fl} of MC containing DI and LS aggregate.

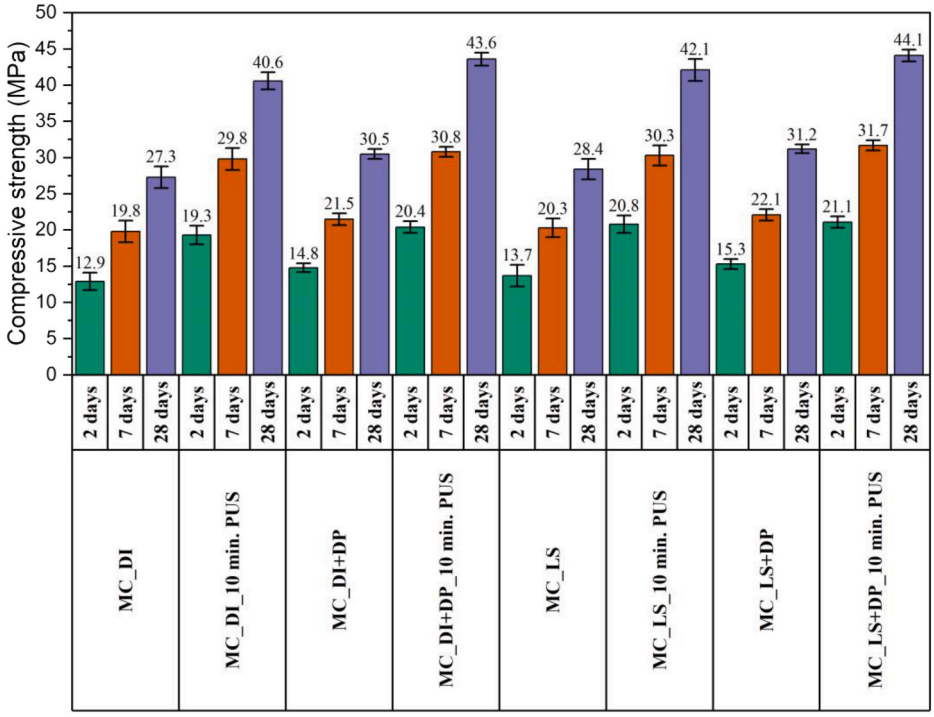

Fig. 4. f_c of MC containing DI and LS aggregate.

It should be noted that fluorescence microscopy and the associated ITZ width measurements were performed exclusively on DP-containing specimens (MC_DI + DP, MC_DI + DP_10 min. PUS, MC_LS + DP, MC_LS + DP_10 min. PUS). Accordingly, the reported baseline ITZ width of approximately 150 μm (MC_LS + DP, without PUS) represents the interfacial condition of a DP-modified matrix before PUS activation, not that of plain unmodified concrete. The comparison of interest quantifying the isolated effect of PUS within the DP-modified system is therefore internally consistent and correctly bounded. The measured baseline ITZ width of approximately 150 μm is consistent with the upper range of values reported in fluorescence microscopy-based ITZ quantification studies [23], and reflects three factors specific to the present system. First, the high w/b ratio of 0.50 promotes localised water film accumulation beneath the aggregate surface, broadening the porosity gradient [25]. Second, unsonicated DP particles (D_{50} = 110 μm) are too coarse to effectively pack within the confined ITZ prior to PUS treatment and may locally disrupt cement particle packing through a secondary wall effect [1]. Third, the chemically active limestone surface promotes dissolution-precipitation reactions that extend microstructural heterogeneity further into the bulk matrix than is typical for inert aggregates, resulting in a broader, more diffuse transition zone [10]. Furthermore, fluorescence microscopy captures the full capillary porosity gradient and therefore systematically yields wider ITZ estimates than nanoindentation-based approaches, which are confined to the mechanically distinct near-interface zone [23]. The broad transition zone visible in Fig. 9a provides direct visual corroboration of this baseline width. The characterisation of the plain concrete ITZ (MC_LS, without DP) is beyond the scope of this study and constitutes a necessary direction for future work to fully decouple the individual contributions of DP and PUS to ITZ width reduction.

Fig. 6 illustrates the method for identifying and quantifying ITZ using fluorescence microscopy combined with digital image analysis. The fluorescence image (Fig. 6a) shows the CM in bright green and aggregates as dark regions; Image-Pro Plus software applies thinning filters to reduce it to its skeleton (Fig. 6b), converting grayscale intensity data into a binary representation of structural boundaries. The final step (Fig. 6c) creates a spatial calibration of the fluorescence intensity moving away from the aggregate surface, mapping how the fluorescent signal changes with distance from the aggregate interface into the bulk paste. The PUS-untreated DI-cement interface (MC_DI + DP, containing DP but without sonication) established baseline microstructural characteristics.

Fluorescence microscopy (Fig. 7a) revealed extensive porosity at the aggregate-paste boundary, with bright green fluorescence indicating the presence of void spaces and microstructural heterogeneity. The skeletonised image (Fig. 7c) demonstrated discontinuous contact between phases with numerous gaps along the interface. The intensity profile (Fig. 7b) exhibited three distinct plateaus corresponding to DI aggregate, ITZ, and bulk CM, with sharp discontinuities indicating abrupt microstructural transitions rather than gradual property gradients.

The application of 10 min. PUS produced a markedly improved DI–CM interface (Fig. 8). Fluorescence microscopy (Fig. 8a) demonstrates substantially reduced porosity compared with the untreated specimen, with far less bright green fluorescence indicating void closure and improved consolidation. Skeletonised analysis (Fig. 8c) reveals more continuous and intimate contact between the DI aggregate and CM, with significantly fewer discrete gaps or debonding zones. The intensity profile (Fig. 8b) shows a more gradual and continuous transition between DI and CM, indicating progressive property changes rather than abrupt discontinuities. Quantitative analysis of the skeletonised image (Fig. 8c) yielded eleven perpendicular ITZ width measurements ranging from 66.6 to 141.3 μm (mean 100.6 ± 26.8 μm, n = 11). The lower measurement count relative to the LS system (n = 13) reflects the stricter perpendicularity criterion applied to DI aggregate boundaries: owing to the irregular, angular surface morphology characteristic of igneous rocks, a greater proportion of boundary segments were excluded to eliminate stereological overestimation [29]. While this strict perpendicularity filtering naturally limits the final number of analyzed measurement frames compared to conventional random-sampling methods, it rigorously prioritizes geometrical accuracy and ensures that the quantified ITZ widths are free from spatial distortion and stereological overestimation [23,29]. The corresponding baseline ITZ width in the MC_DI + DP specimen (Fig. 7c), determined by spatial intensity calibration analysis of the skeletonised image using the same

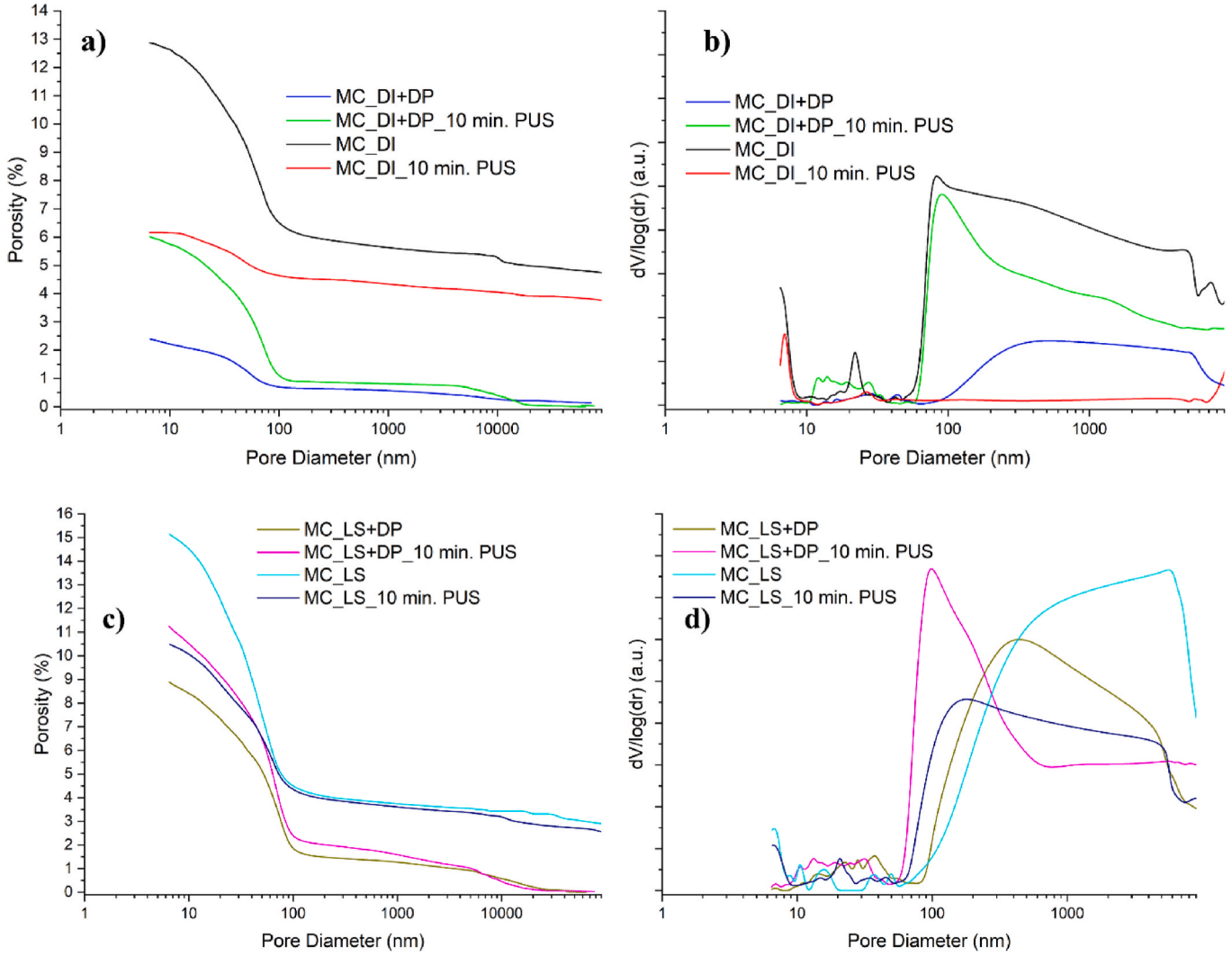

Fig. 5. The influence of PUS on the pore size distribution in concrete specimens: total porosity (a, c) and differential pore size distribution (b, d).

Table 5
Porosity and pore size distribution in concrete and rock aggregate specimens.

Aggregate types	Concrete and rock notation, sonication	Total porosity [%]	Porosity distribution [%] in the range		
			10-100 nm	100-1000 nm	>1000 nm
DI	MC_DI	12.86	6.67	0.97	5.22
	MC_DI_10 min. PUS	6.16	1.59	0.52	4.05
	MC_DI + DP	2.39	1.71	0.42	0.26
	MC_DI + DP_10 min. PUS	6.01	5.08	0.57	0.36
	DI_stone	2.52	0.80	0.29	1.43
LS	MC_LS	15.14	10.94	0.77	3.43
	MC_LS_10 min. PUS	10.49	6.26	1.04	3.19
	MC_LS + DP	8.89	7.11	1.22	0.56
	MC_LS + DP_10 min. PUS	11.24	9.05	1.77	0.42
	LS_stone	7.02	0.11	0.24	6.67

perpendicular-trajectory methodology applied to Fig. 8c, was approximately 144 μm, consistent with a ~30% reduction induced by PUS treatment.

It should be noted that due to the highly diffuse, irregular, and broad nature of the unsonicated ITZ driven by the coarse unactivated DP particles and high w/b ratio, extracting a large statistical sample of strictly perpendicular measurement trajectories was geometrically limited. This limitation arises not primarily from the difficulty of identifying perpendicular orientations, but from the diffuse nature of the intensity gradient itself: in the absence of a sharp fluorescence discontinuity, the aggregate-paste boundary cannot be unambiguously localized to a discrete reference point, introducing an additional source of positional uncertainty that precludes rigorous per-trajectory measurement at the same level of confidence achieved for the sharply defined, PUS-densified interfaces. Therefore, representative spatial intensity profiles were used to establish the approximate baseline widths (~144 μm and ~150 μm), whereas the highly consolidated, sharper interfaces of the PUS-treated specimens permitted robust statistical sampling (mean ± standard deviation).

Notably, the coefficients of variation of the DI and LS systems were nearly identical (26.6% vs. 26.3%, respectively). This convergence suggests that the spatial variability of ITZ width, governed primarily by local variations in aggregate surface roughness and cement particle packing efficiency, is an intrinsic geometric characteristic of the aggregate-paste system that PUS narrows proportionally but does not spatially homogenise further, regardless of whether the dominant bonding mechanism is chemical-physical (LS) or purely physical (DI).

The LS–cement interface without PUS (Fig. 9) exhibits fundamentally different characteristics from those of DI, reflecting the distinct

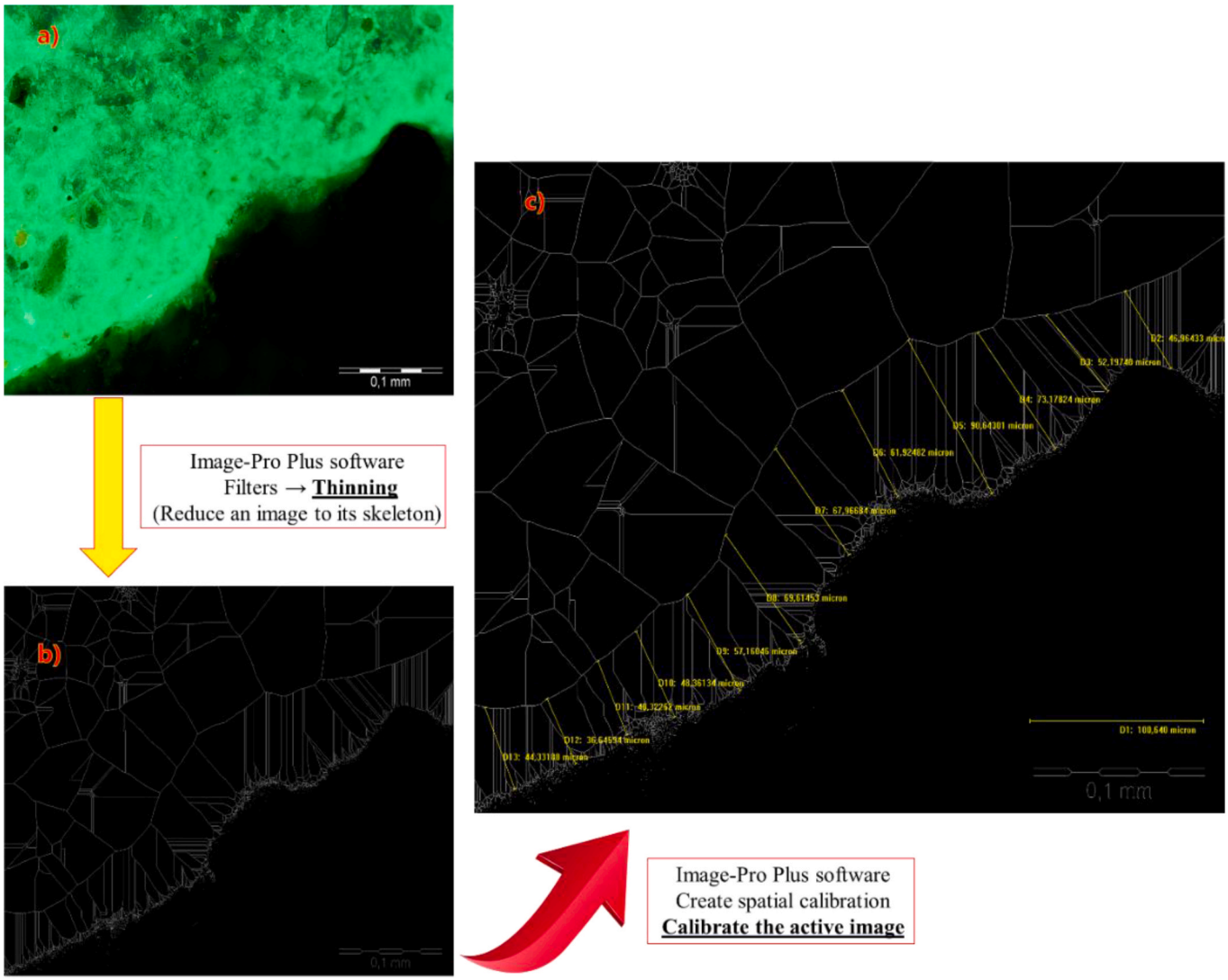

Fig. 6. Flowchart of the method for identifying and quantifying the ITZ.

chemical and physical nature of calcareous aggregates. Fluorescence microscopy (Fig. 9a) reveals extensive porosity distributed throughout a broad transition zone, diffuse and extending into the CM rather than forming the discrete gap seen at the DI interface. The skeletonised image (Fig. 9c) demonstrates a complex morphology with irregular boundaries and extensive microcracking patterns. The intensity profile (Fig. 9b) shows a broader, more gradual transition with persistently elevated intensity throughout the ITZ, indicating continued microstructural heterogeneity. PUS treatment of the LS system produced the most dramatic microstructural improvements observed in this study (Fig. 10). Fluorescence microscopy (Fig. 10a) reveals exceptional densification throughout the interfacial region, with the CP conforming intimately to the LS surface topography. Skeletonised analysis (Fig. 10c) shows highly continuous contact with minimal discontinuities. The intensity profile (Fig. 10b) demonstrates a substantially narrowed transition zone (37–91 μm, mean 57.4 ± 15.1 μm, n = 13 perpendicular aggregate boundaries) with steeper gradients, indicating that properties transition more rapidly from LS to bulk paste, with a markedly reduced region of compromised performance.

3.5. Microindentation data

Microindentation measurements were performed exclusively on DP-containing specimens (MC_DI + DP, MC_DI + DP_10 min. PUS, MC_LS + DP, MC_LS + DP_10 min. PUS); all reported changes therefore reflect the isolated effect of PUS within the DP-modified system, with the independent contribution of DP remaining mathematically undecoupled, a necessary direction for future characterisation. For the untreated DI system (MC_DI + DP), indentation hardness values of 278.2 MPa (ITZ), 281.7 MPa (CM), and 2358.6 MPa (aggregate), and EM of 17.8, 19.1, and 81.8 GPa, respectively (Table 6), reflect poor cement particle packing, elevated local w/c ratio, and the complete absence of chemical bonding at the hard, inert DI surface. Following PUS treatment (MC_DI + DP_10 min. PUS), CM hardness increased modestly by 1.6% (281.7 → 286.1 MPa) and EM by 3.1% (19.1 → 19.7 GPa). The apparent decrease in ITZ indentation hardness (278.2 → 193.4 MPa) is interpreted as a consequence of ITZ narrowing (~30%: from ~144 μm to 100.6 ± 26.8 μm, n = 11) rather than true material weakening: as the diffuse gradient compresses into a sharper transition, indents nominally assigned to the ITZ position increasingly sample the heterogeneous aggregate–paste boundary rather than a spatially distinct weak phase.

The untreated LS system (MC_LS + DP) yielded hardness values of 350.6 MPa (ITZ), 357.1 MPa (CM), and 1147.1 MPa (aggregate), and EM of 21.1, 21.3, and 45.1 GPa, respectively (Table 6). The near-identical ITZ and CM hardness values reflect the chemically active calcareous surface, which undergoes partial dissolution-precipitation within a porous, water-rich microstructure, resulting in a diffuse but weakly consolidated interface. PUS treatment (MC_LS + DP_10 min. PUS)

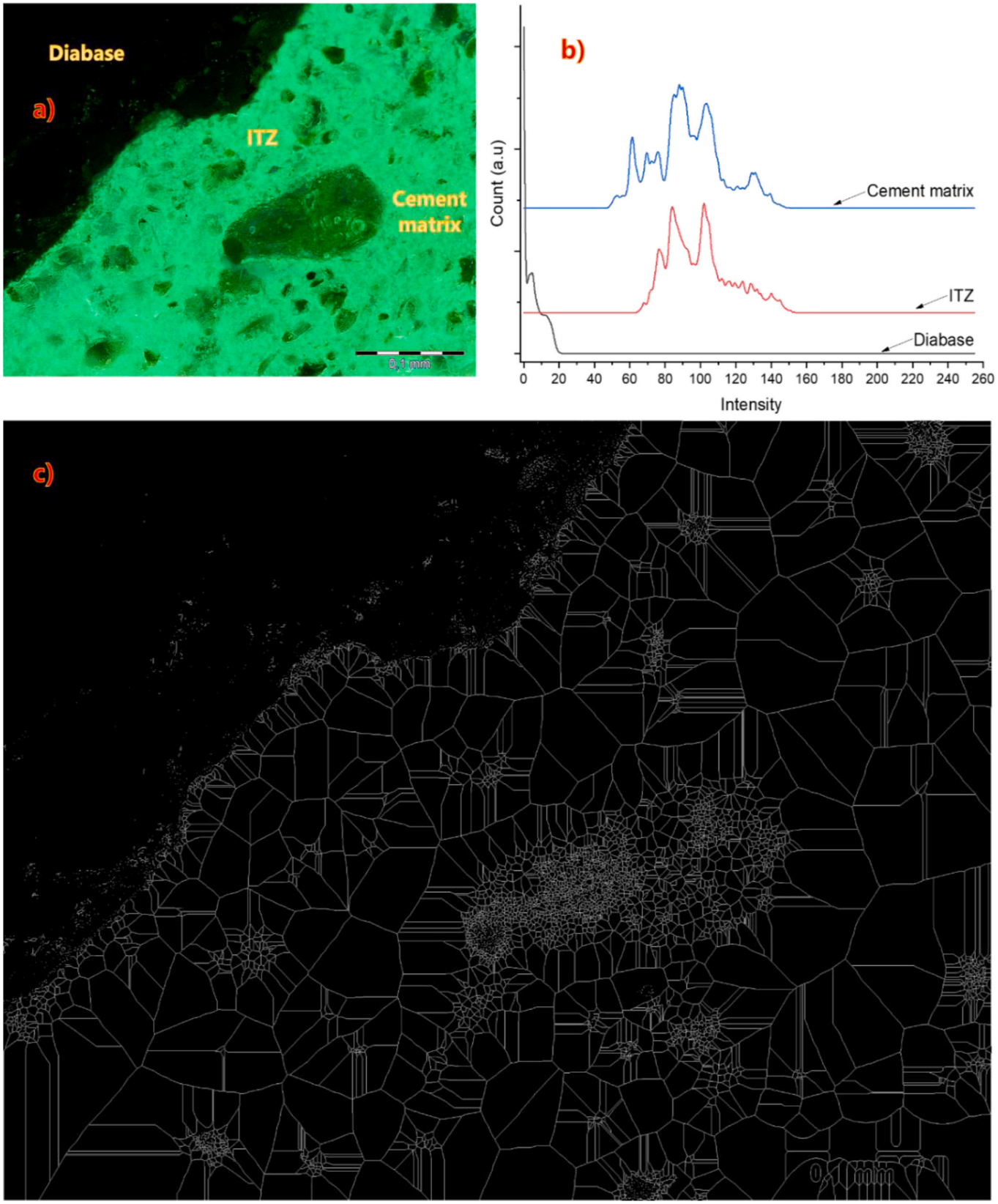

Fig. 7. Evaluation of MC_DI + DP specimen (without sonication): (a) fluorescence microscopy image (UV), (b) spatial intensity calibration, and (c) skeletonised image.

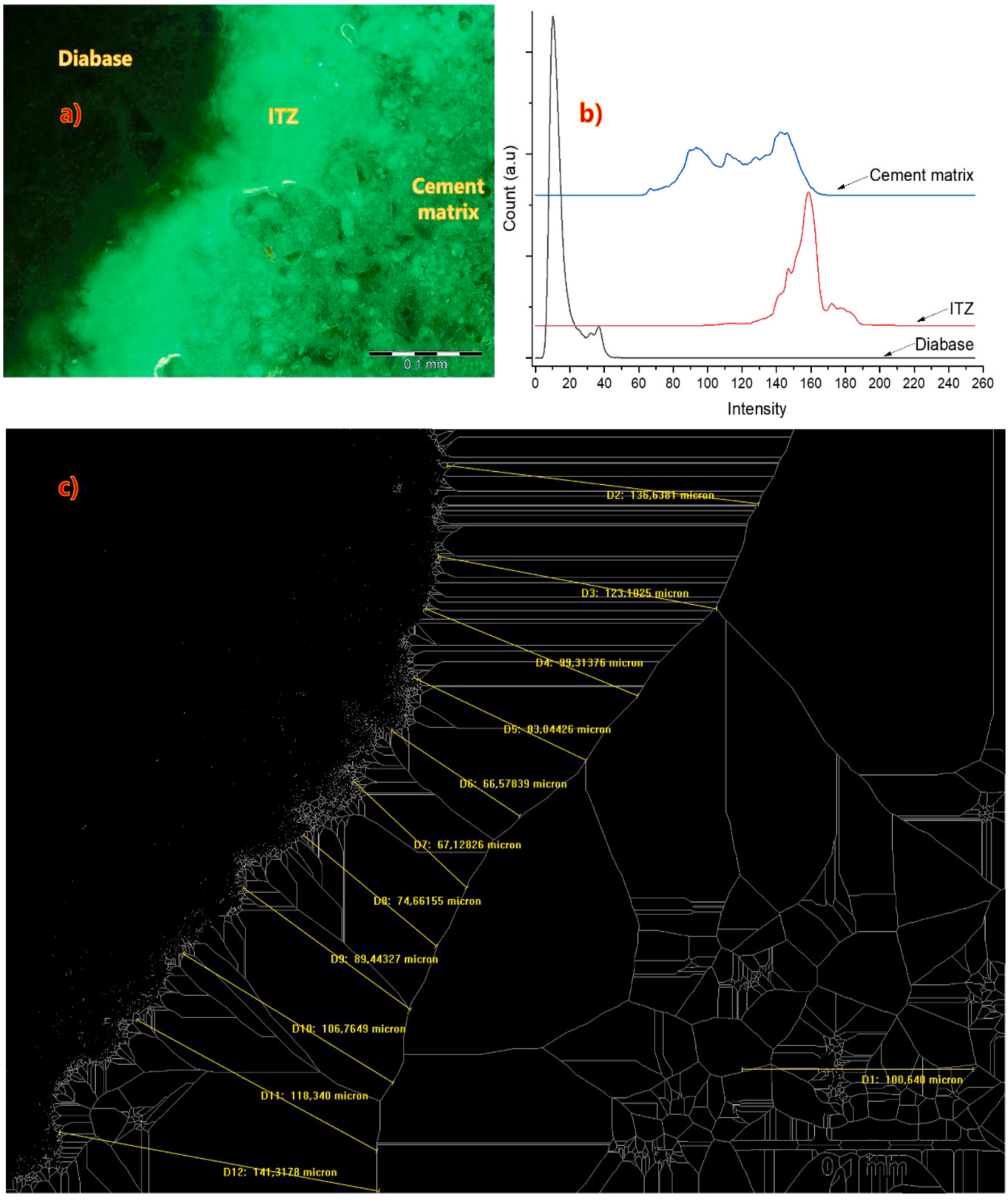

Fig. 8. Evaluation of MC_DI + DP_10 min. PUS specimen: (a) fluorescence microscopy image (UV), (b) spatial intensity calibration, and (c) skeletonised image.

produced the most dramatic improvements: CM hardness increased by 27.4% (357.1 → 455.1 MPa) and EM by 10.3% (21.3 → 23.5 GPa) - the largest enhancements observed across all conditions. The slight apparent increase in LS aggregate hardness (1147.1 → 1217.7 MPa) and modulus (45.1 → 47.3 GPa) most likely reflects natural mineralogical variation among tested particles rather than a fundamental alteration of the solid rock. Consistently, the decrease in apparent ITZ indentation values reflects the ~62% width narrowing confirmed by fluorescence microscopy (from ~150 μm to 57.4 ± 15.1 μm, n = 13), with the 27.4% CM hardness gain directly demonstrating pronounced pozzolanic C–S–H

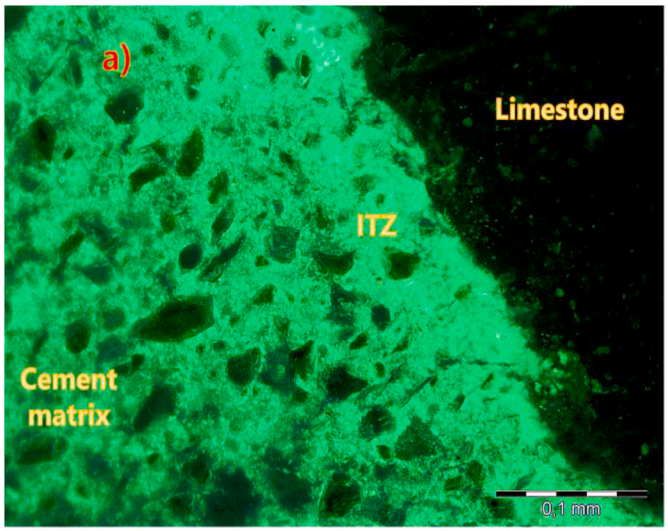

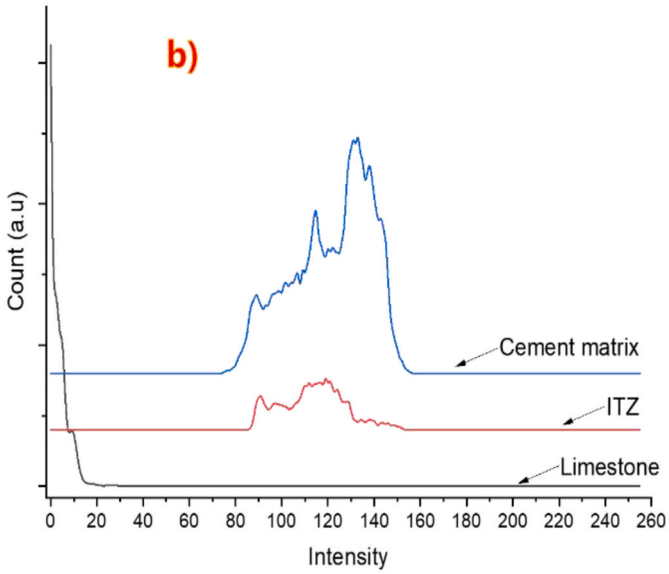

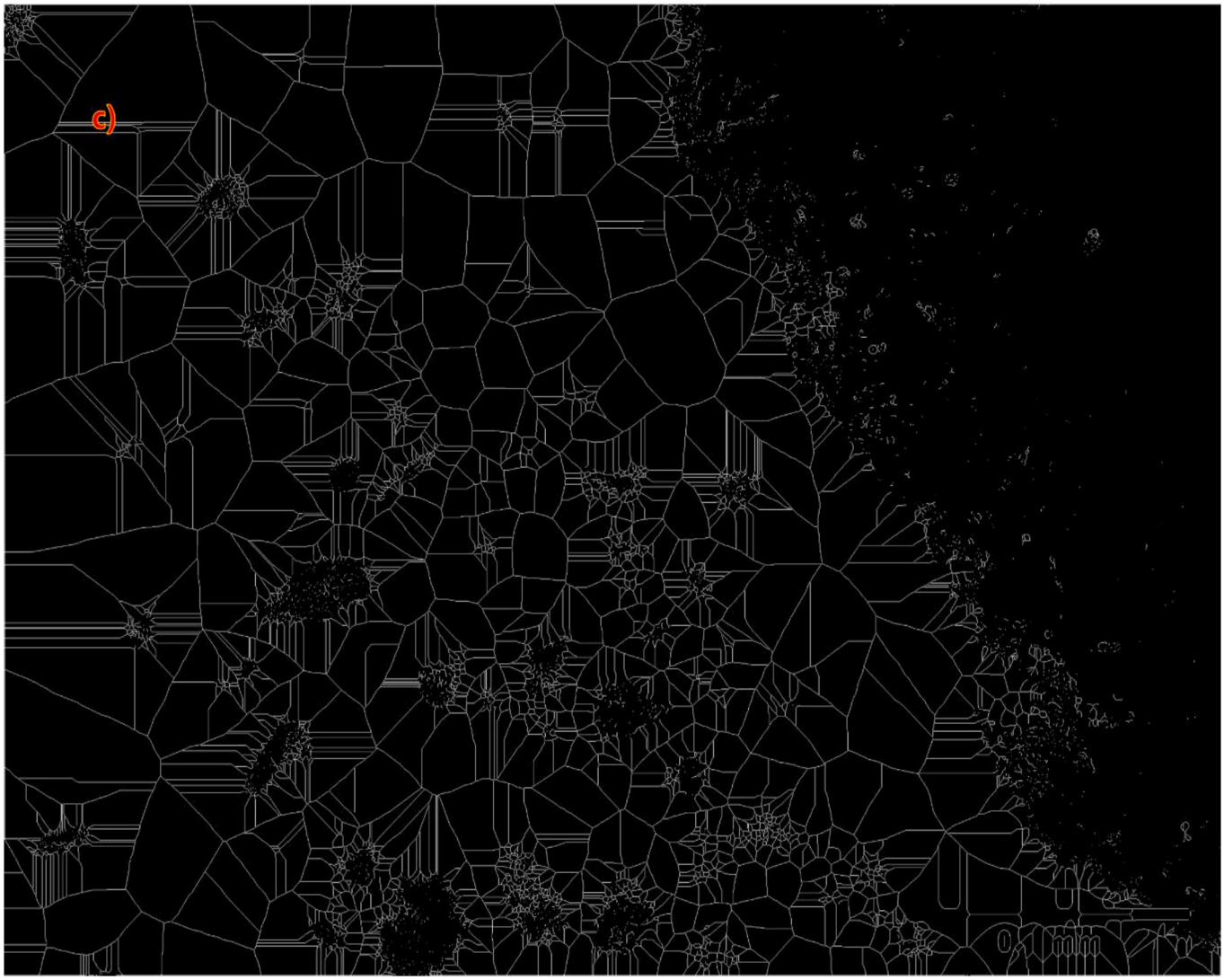

Fig. 9. Evaluation of MC_LS + DP specimen (without sonication): (a) fluorescence microscopy image (UV), (b) spatial intensity calibration, and (c) skeletonised image.

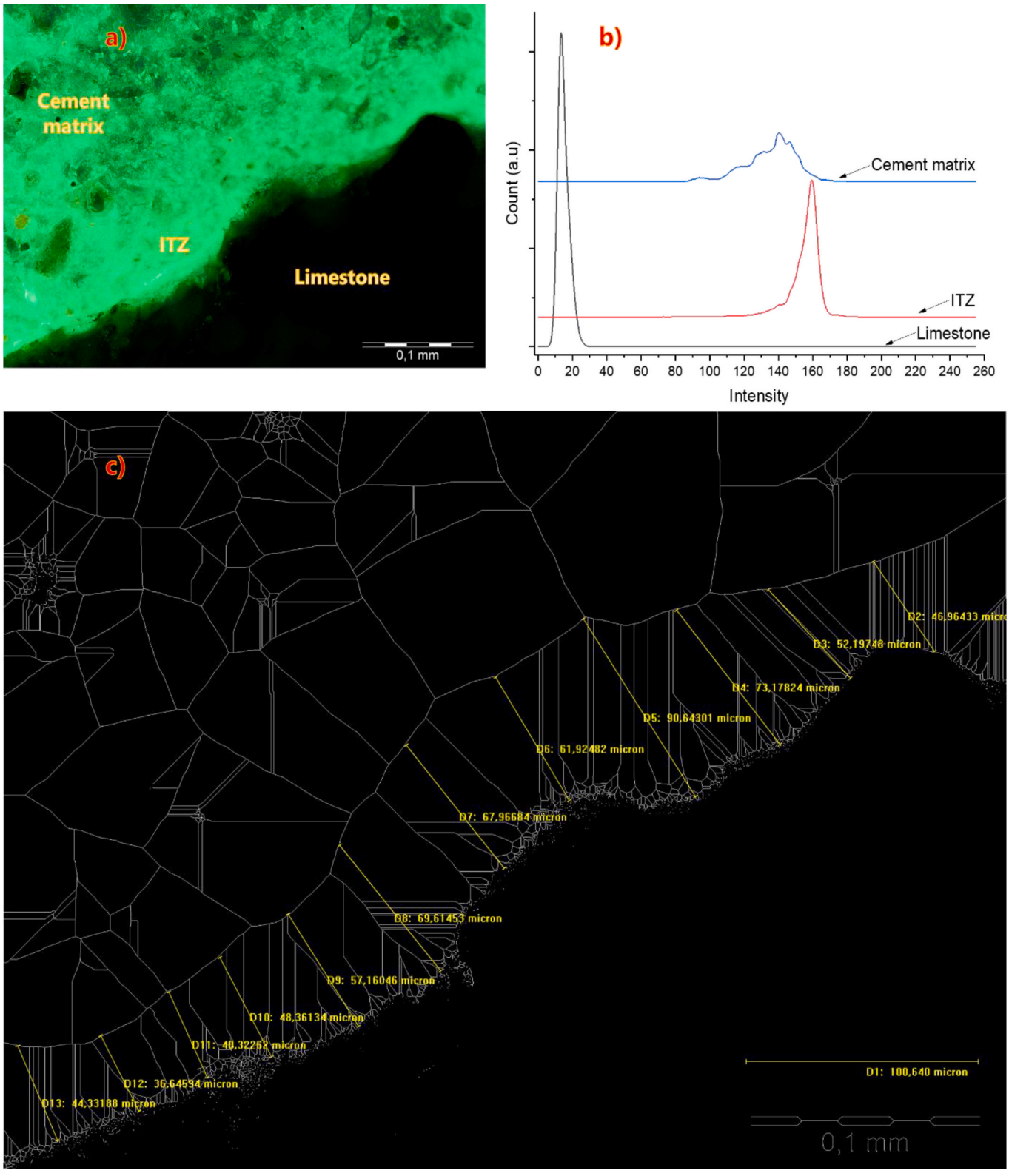

Fig. 10. Evaluation of MC_LS + DP_10 min. PUS specimen: (a) fluorescence microscopy image (UV), (b) spatial intensity calibration, and (c) skeletonised image.

densification at the calcareous interface achieved by the DP + PUS combination.

In summary, DI systems achieve moderate improvements primarily through physical consolidation mechanisms - particle dispersion, void filling, and improved mechanical interlocking constrained by the complete absence of chemical compatibility at the hard, inert silicate surface. LS systems achieve superior improvements through synergistic chemical-physical bonding: in addition to the physical benefits observed in DI, enhanced chemical reactivity, improved ion transport, better surface preparation on the reactive calcareous substrate, and synergistic interactions between LS dissolution-precipitation and DP pozzolanic reactions collectively produce the pronounced CM hardening and ITZ

Table 6
Microindentation data in selected areas of polished concrete sections.

		Concrete and rock notation, sonication			
		MC_DI + DP	MC_DI + DP_10 min. PUS	MC_LS + DP	MC_LS + DP_10 min. PUS
Indentation hardness [MPa]	Aggregate	2358.6 ± 59.9	2398.2 ± 69.3	1147.1 ± 65.6	1217.7 ± 72.3
	ITZ	278.2 ± 45.8	193.4 ± 34.9	350.6 ± 46.2	318.1 ± 32.0
	CM	281.7 ± 47.7	286.1 ± 52.1	357.1 ± 48.5	455.1 ± 52.1
Elastic modulus [GPa]	Aggregate	81.8 ± 1.8	82.9 ± 2.1	45.1 ± 2.0	47.3 ± 2.2
	ITZ	17.8 ± 1.7	16.9 ± 1.4	21.1 ± 1.4	19.6 ± 1.8
	CM	19.1 ± 1.5	19.7 ± 1.6	21.3 ± 1.5	23.5 ± 1.3

narrowing observed.

3.6. SEM observations

SEM characterisation was performed at 7 d to capture the early-age ITZ microstructure before long-term pozzolanic C-S-H deposition obscures the initial physical effects of PUS. In the untreated DI system (Fig. 11a), a distinct aggregate–CM boundary with visible porosity, elongated microcracks running parallel to the aggregate surface, and a wide heterogeneous transition zone collectively indicate pronounced mechanical weakness and potential failure initiation sites. Following PUS treatment (Fig. 11b), the DI–CM interface appeared markedly tighter, with substantially reduced gap formation, a denser CM immediately adjacent to the aggregate surface, and improved hydration product penetration into surface irregularities. In the untreated LS system (Fig. 12a), the interface was characterised by diffuse, deeply penetrating porosity and a partially dissolved aggregate surface - consistent with active carbonate–alkaline pore-solution interaction - yet remained weak and highly porous, lacking adequate consolidation. PUS treatment of the LS system (Fig. 12b) produced the most dramatic improvement: the CM penetrated deeply into the aggregate surface texture, forming an interdigitated, mechanically interlocked interface with markedly reduced porosity and substantially greater microstructural homogeneity. Collectively, these observations are consistent with PUS effectively densifying the DP-modified ITZ through a combination of physical consolidation and enhanced chemical reactivity, the latter being independently supported by the R^3 calorimetry results (Section 3.1). The 7 d SEM results capture the initial densification achieved by PUS-induced defoaming and particle redistribution; continued PR beyond 7 d is expected to progressively fill the residual capillary porosity visible in Fig. 11a and 12a, ultimately yielding the denser 28 d microstructure consistent with the MIP and microindentation data reported in Sections 3.3 and 3.5.

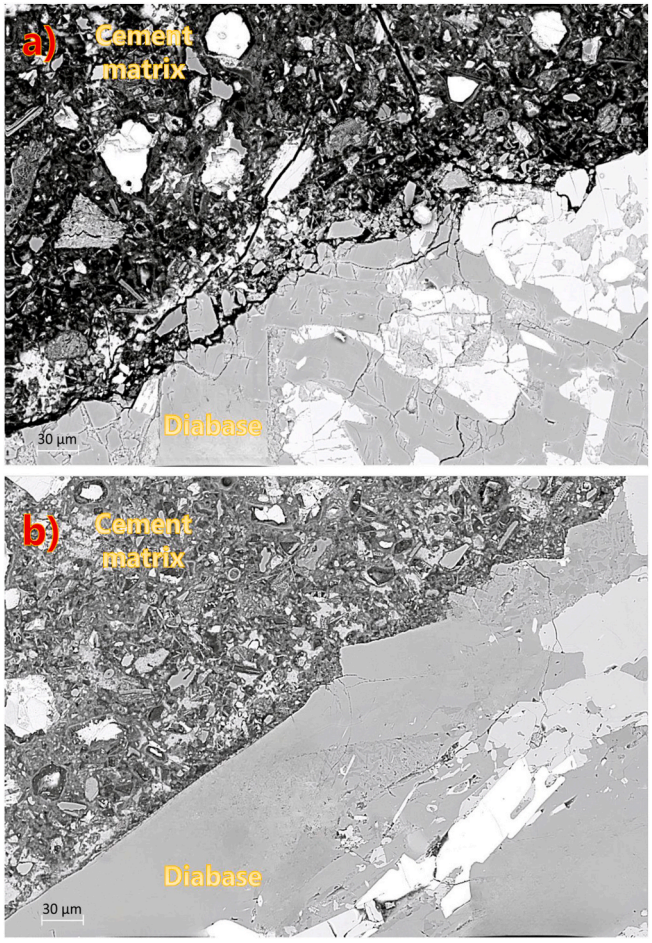

Fig. 11. SEM images of the DI–CP ITZ: (a) MC_DI + DP without PUS treatment and (b) MC_DI + DP_10 min. PUS - both after 7 d of curing.

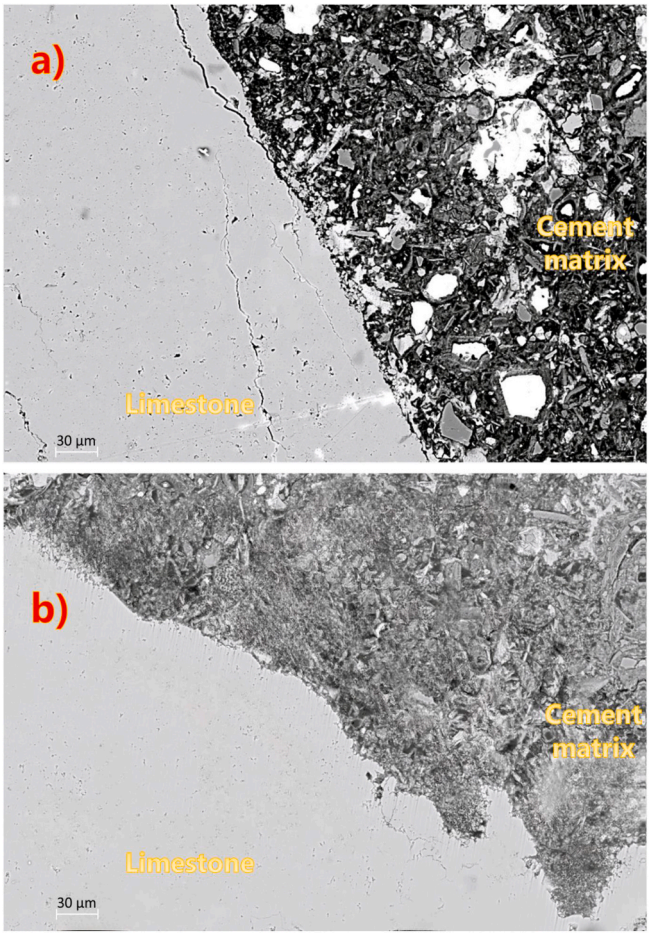

Fig. 12. SEM images of the LS–CP ITZ: (a) MC_LS + DP without PUS treatment and (b) MC_LS + DP_10 min. PUS - both after 7 d of curing.

4. Discussion

The combined DP + PUS processing route delivered exceptional composite mechanical performance, compressive strengths of 43.6 MPa (~60% above the DI control) and 44.1 MPa (~55% above the LS control) while simultaneously incorporating 20% cement replacement, demonstrating that acoustic activation of an SCM matrix phase constitutes a viable composite engineering strategy for producing high-performance, reduced-clinker particulate composites. Within the composite performance hierarchy, PUS emerged as the primary driver of macroscopic strength: PUS treatment alone (without DP) already achieved 40.6 MPa (DI) and 42.1 MPa (LS) at 28 d, with DP supplementation providing an additional 2–3 MPa gain (4.7% for LS, 7.4% for DI). However, within the microstructural hierarchy of composite improvement mechanisms, the roles are complementary and non-interchangeable: DP acts as the primary agent for eliminating critical Griffith-type macropore defects (>1000 nm) at the matrix–inclusion interface, while PUS is the primary driver of bulk matrix densification and ITZ narrowing. The 10 min PUS duration identified as optimal is sufficiently short to be compatible with industrial composite fabrication cycle times, providing a practical processing parameter for scale-up.

4.1. Hydration kinetics and defoaming mechanisms under sonication

The progressive increase in DP reactivity with PUS duration (Section 3.1) can be explained through the principles of acoustic cavitation. When PUS is applied to the fresh paste, the alternating acoustic pressure induces stable cavitation. Contemporary sonochemical theories indicate that oscillating bubbles generate secondary Bjerknes forces, compelling trapped air pockets to quickly merge and escape upward. Critically, the sonofragmentation of DP particles documented in the companion study [43] provides a second, independent densification pathway operating in parallel with acoustic defoaming. After 10 min of PUS, the D_{50} of the 125-250 μm DP fraction was reduced from 110.0 μm to 9.7 μm, and the specific surface area of the hardened paste increased by 69% relative to the untreated reference [43]. Particles of this size (D_{50} < 10 μm) are comparable in fineness to Portland cement (typical $D_{50} \approx$ 10-15 μm) and are therefore fully capable of penetrating and filling the ITZ. This dual action - macropore removal by acoustic defoaming and ITZ gap filling by sonofragmented DP explains why the mechanical gains exceed what either mechanism alone would predict. This process provides a robust physical mechanism for void removal, resulting in a highly compacted microscopic matrix [37]. Alongside this densification, the acoustic impact provides sufficient energy to overcome initial reaction constraints, promoting the rapid, localized formation of C-S-H and portlandite (CH) crystal nuclei, which act as nucleation seeds and substantially shorten the induction period [38]. Furthermore, the intense acoustic forces efficiently drive out entrapped air voids and physically unclog the intrinsic pores of DP, exponentially increasing its active specific surface area [37]. This framework directly validates the MIP-measured pore refinement (capillary pores 10–100 nm: 6.67% → 1.59%; Table 5) and the early-age strength improvements at 2 d (f_{fl}: +21%, f_c: +50%; Figs. 3 and 4). Therefore, the true synergy of the DP + PUS system lies in a coupled physical-chemical mechanism. While the incorporation of DP provides the physical bulk necessary to fill critical >1000 nm macropore defects, the PUS treatment acts as a dynamic catalyst. It not only sonofragments the initially coarse DP particles (reducing the D_{50} from 110.0 μm to 9.7 μm) to geometrically enable their deep penetration into the confined ITZ, but also simultaneously accelerates their pozzolanic reactivity, as evidenced by the 12.8% increase in cumulative heat release. PUS essentially prepares the DP geometry to perfectly match the scale of the interfacial defects.

4.2. The influence of aggregate mineralogy on interfacial bonding

The contrasting response of LS and DI to identical DP + PUS treatment (LS: +27.4% CM hardness, ~62% ITZ narrowing; DI: +1.6% hardness, ~30% narrowing; Section 3.5) is governed by the distinct surface free energies and chemical compositions of the two aggregates [40,42]. LS, a calcareous substrate with a non-polar surface and highly alkaline components, is consistent with promoting oriented crystallisation of C–S–H and portlandite through carbonate–calcium chemical affinity directly at the interface [39,40]; its lower Mohs hardness and higher intrinsic porosity further allow PUS to force the activated DP-modified paste deep into the aggregate's surface pores, enabling synergistic chemical-physical bonding. Conversely, DI is a highly polar, inert igneous rock where bonding relies predominantly on mechanical interlocking [40,73]; PUS therefore improved physical consolidation around DI aggregates, but the absence of chemical compatibility precluded the dramatic hardness enhancement observed in LS specimens.

The pore size distribution of LS systems conclusively illustrates why total porosity is an insufficient predictor of macroscopic strength. Despite MC_LS + DP_10 min. PUS exhibiting higher total porosity (11.24%) than its unsonicated counterpart (8.89%), it achieved the highest f_c (44.1 MPa) - a 12.9 MPa gain. Two complementary mechanisms reconcile this observation: (i) the DP-driven selective elimination of large macropores (≥1000 nm, reduced to 0.42%), independently linked to the aggregate-paste interface through correlative fluorescence and SEM imaging (Sections 3.3, 3.4, 3.6), is consistent with the removal of Griffith-type stress concentrators, raising fracture toughness disproportionately to their volume fraction; and (ii) the concurrent 27.4% increase in CM hardness adjacent to the ITZ is consistent with pozzolanic C–S–H densification acting as a co-governing mechanism, although direct phase-compositional confirmation was not performed in this study (see Section 4.2 concluding remarks). The observed increase in 10–100 nm pore content (7.11% → 9.05%) is attributed to the combined effects of additional C-S-H gel porosity generated through pozzolanic reaction, refinement of larger capillary pores into this size range, and physical unclogging of intrinsic DP pores by acoustic cavitation (Section 3.3), collectively contributing to matrix stiffening rather than weakening. Future Digital Image Correlation (DIC) or acoustic emission (AE) measurements during mechanical loading are recommended to trace fracture initiation sites and definitively apportion the relative contributions of these mechanisms, particularly regarding whether crack initiation bypasses the finer pore regions entirely. This 'porosity paradox' definitively proves that the spatial distribution and specific size of interfacial defects are vastly more critical to macro-scale failure mechanics than the total void volume. The DP + PUS treatment effectively redistributes the internal architecture: it replaces fatal, Griffith-type macro-stress concentrators (>1000 nm) with a highly dispersed network of innocuous nanoscale gel pores (10-100 nm) generated by the accelerated pozzolanic reaction and capillary refinement. Consequently, while overall porosity increased slightly due to micro-level C-S-H gel reorganisation and deep paste penetration into aggregate surface pores, the critical load-bearing interfacial zones were markedly reinforced through pozzolanic densification, overcoming the total porosity deficit and producing the net macroscopic strength gains observed. Furthermore, while the current micromechanical and R^3 calorimetric data robustly infer localized pozzolanic densification, future investigations utilizing spatially resolved interfacial chemical characterization such as high-resolution SEM-EDS mapping or nano-XRD are essential to directly verify the proposed phase-compositional changes and the exact stoichiometry of the C-S-H formed at the respective aggregate boundaries [74,75].

4.3. Micro-to-Macro upscaling and ITZ percolation modelling

The mechanical tests revealed a notable ~59% improvement in f_c relative to the unmodified concrete control and a 50–62% improvement in f_{fl}, despite 20% cement replacement. To analytically support the hypothesis that the measured local modifications contribute to this macroscopic strengthening, our 2D morphological and

microindentation data are contextualized within 3D spatial and micromechanical homogenization frameworks.

4.3.1. 3D ITZ volume fraction and disconnection of percolated networks

The reduction in the apparent 2D ITZ thickness (from ~150 μm to a mean of ~57.4 μm, range 37–91 μm) measured via fluorescence microscopy in the current study has significant implications for the 3D topology of the concrete matrix. In standard concrete mixtures, a wide ITZ significantly increases the "spacing factor" between aggregates, leading to geometric overlap (percolation) of adjacent weak ITZ regions and creating interconnected pathways for rapid crack propagation [24,26]. To mathematically justify the macroscopic strengthening, the true 3D volume fraction of the ITZ (V_{ITZ}) can be analytically predicted from our measured spatial boundaries using the nearest-surface distribution function (the Lu-Torquato model) [26,67,72]:

$$V_{ITZ} = 1 - V_{agg} - V_{bp} \quad (1)$$

$$V_{bp} = (1 - V_{agg})\exp\left[-\pi N_v \left(e \cdot t_{ITZ} + d \cdot t_{ITZ}^2 + g \cdot t_{ITZ}^3\right)\right] \quad (2)$$

Table 7 summarizes the model's input parameters. The exponential dependence on the ITZ thickness (t_{ITZ}) in this model mathematically demonstrates that the ~62% reduction in ITZ width achieved via PUS treatment in the LS specimens in our research significantly reduces the total 3D volume of the weak phase. More importantly, this narrowing substantially disrupts the percolated weak network. Consequently, the isolated, narrowed ITZs no longer dominate the global failure mechanism, forcing macroscopic cracks to propagate through the denser bulk matrix [26,27]. The step-by-step calculation results are presented in Table 8.

The 3D ITZ volume fraction, therefore, decreases from 3.0% to 1.1% - a 63% reduction consistent with the measured 2D width data. It should be acknowledged that the Lu–Torquato model is applied here with a monodisperse sphere approximation (R = 3.71 mm, volume-weighted mean of the 4-8 mm and 8-12.5 mm fractions) rather than the polydisperse formulation. For a bimodal aggregate blend with a 2:1 size ratio, the monodisperse approximation may underestimate V_{ITZ} by up to 10–15% [67]. Additionally, the V_{ITZ} values reported are sensitive to the measured t_{ITZ}: a ±30% uncertainty in t_{ITZ} propagates to a V_{ITZ} range of approximately 0.5–1.5% (PUS-treated) and 1.8–4.5% (baseline), reflecting the exponential dependence in Eq. (2). These limitations notwithstanding, the directional conclusion - that PUS treatment substantially reduces the 3D volume of the weak ITZ phase - remains robust. This dramatic decrease in V_{ITZ} indicates that the percolated weak network connecting adjacent aggregate particles through overlapping ITZ shells is substantially disrupted by PUS treatment. Using the percolation threshold criterion [76], which for a random sphere system at V_{agg} = 0.568 predicts percolation onset when the ITZ shell volume fraction exceeds approximately 1–2%, the baseline V_{ITZ} = 3.0% is consistent with a percolated network, while the PUS-treated V_{ITZ} = 1.1% falls below this threshold suggesting the network is indeed disconnected after treatment, forcing macroscopic crack propagation through the denser bulk matrix rather than the ITZ [26,27]. Although the proximity of V_{ITZ} to the 1-2% critical range precludes a definitive conclusion regarding full network disconnection, this topological shift significantly impedes continuous crack propagation along the ITZ and increasingly forces macroscopic fracture through the denser bulk matrix.

Table 7
Input parameters for the Lu–Torquato model (LS micro-concrete, monodisperse sphere approximation).

Parameter	Symbol	Value (LS System)
Aggregate volume fraction	V_{agg}	0.568
Volume-weighted mean aggregate radius	R	3.71 mm
Number density of aggregate particles	N_v	2.66×10^6 m^{-3}
Geometric coefficient e = $4R^2$	e	5.50×10^{-5} m^2
Geometric coefficient d = 4R	d	1.48×10^{-2} m
Geometric coefficient g = 4/3	g	1.333

Table 8
Step-by-step Lu–Torquato calculations and key outcomes for the LS system.

Calculation Step	Baseline (no PUS)	PUS-Treated
ITZ thickness (t_{ITZ})	150 μm	57.4 μm
Bulk paste volume fraction (V_{bp}) [Eq. (2)]	0.402	0.421
3D ITZ volume fraction (V_{ITZ}) [Eq. (1)]	0.030	0.011
V_{ITZ} (%)	3.0%	1.1%
Reduction in V_{ITZ}	(3.0−1.1)/3.0 = 63%	

While the monodisperse sphere approximation introduces a recognized underestimation of the absolute V_{ITZ} compared to a fully polydisperse model, this systematic simplification does not invalidate the study's core topological conclusion. The relative reduction of V_{ITZ} by 63% (from 3.0% to 1.1%) is independent of this baseline shift. This massive relative decrease serves as a robust mathematical demonstration that PUS treatment severely disrupts the mechanically percolated weak ITZ network, drastically reducing its propensity for percolation and effectively altering the global failure trajectory of the material.

4.3.2. Micromechanical homogenization (Mori-Tanaka scheme)

While the Lu-Torquato model explains the volumetric reduction of defects, the actual stiffness and strength gains of the composite must be justified by the local mechanical improvements. The microindentation tests in the present study mapped a 1.6% to 27.4% increase in local CM hardness and a 3.1% to 10.3% increase in the EM of the CM following PUS treatment. By using the Mori-Tanaka homogenization scheme, the concrete composite can be modelled as a two-phase composite in which aggregate inclusions are embedded in the CM, whose measured EM reflects the integrated effect of ITZ densification at the paste level [31,77,78]. Table 9 lists the elastic properties that were used as input parameters. The local properties of these phases strictly govern the homogenized EM of the concrete (E_{hom}):

$$E_{hom} = \frac{9k_{hom}\tau_{hom}}{3k_{hom} + \tau_{hom}} \quad (3)$$

The composite's shear modulus (τ_{hom}) and bulk modulus (k_{hom}) are obtained from:

$$k_{hom} = \frac{\sum V_i k_i \left(1 + A_r\left(\frac{k_i}{k_r} - 1\right)\right)^{-1}}{\sum V_i \left(1 + A_r\left(\frac{k_i}{k_r} - 1\right)\right)^{-1}} \quad (4)$$

Table 9
Step-by-step Mori–Tanaka calculations and predicted composite EM.

Calculation Step	Before PUS (MC_LS + DP)	After PUS (MC_LS + DP_10 min)
CM elastic modulus	21.3 GPa	23.5 GPa
LS elastic modulus	45.1 GPa	47.3 GPa
Paste bulk modulus	11.83 GPa	13.06 GPa
Paste shear modulus	8.88 GPa	9.79 GPa
LS bulk modulus	30.07 GPa	31.53 GPa
LS shear modulus	18.04 GPa	18.92 GPa
Homogenized bulk modulus (k_{hom}) [Eq. (4)]	19.60 GPa	21.09 GPa
Homogenized shear modulus (τ_{hom}) [Eq. (5)]	13.13 GPa	14.10 GPa
Composite elastic modulus (E_{hom}) [Eq. (3)]	32.2 GPa	34.6 GPa
Predicted increase in E_{hom}	(34.6 − 32.2)/32.2 = +7.5%	

$$\tau_{hom} = \frac{\sum V_i \tau_i \left(1 + B_r\left(\frac{\tau_i}{\tau_r} - 1\right)\right)^{-1}}{\sum V_i \left(1 + B_r\left(\frac{\tau_i}{\tau_r} - 1\right)\right)^{-1}} \quad (5)$$

Where indices r and i refer to the reference bulk paste and inclusion phases (aggregate and ITZ), respectively; V_i represents the volume fraction calculated from the Lu-Torquato model above. Specifically, for spherical inclusions in the Mori–Tanaka scheme: $A_r = (3k_r)/(3k_r + 4\tau_r)$ and $B_r = (6(k_r + 2\tau_r))/(5(3k_r + 4\tau_r))$, where k_r and τ_r are the bulk and shear moduli of the reference matrix phase, respectively [78]. The scientific coherence of the current investigation lies in the synergistic combination of these mathematical frameworks. The PUS treatment simultaneously decreases the volume fraction of the weak phase (V_i in the ITZ decreases via pore dredging and thickness reduction) while increasing its intrinsic mechanical load-bearing capacity (k_i and τ_i increase due to enhanced pozzolanic C-S-H precipitation), as confirmed by our microindentation results [78]. Because the nonlinear stress-strain behavior and quasi-brittle failure of concrete are mathematically dictated by the local tensile strength and stiffness of these interfacial shells [17,30], the application of these homogenization models strongly supports the conclusion that the exceptional macroscopic strength gains recorded during testing are a direct, physically justified consequence of the ultrasonically densified ITZ.

The Mori–Tanaka scheme predicts a 7.5% increase in composite EM (32.2 → 34.6 GPa) resulting from PUS treatment. PUS simultaneously reduces V_{ITZ} (ITZ volume fraction: 3.0% → 1.1%, corresponding to a ~62% reduction in ITZ width from ~150 μm to 57.4 μm) and increases the intrinsic mechanical properties of the CM adjacent to the ITZ (E: 21.3 → 23.5 GPa; k: 11.83 → 13.06 GPa; G: 8.88 → 9.79 GPa) due to enhanced pozzolanic C-S-H precipitation [78]. The complete multi-scale performance summary, integrating all experimental and modelling results for the LS system, is presented in Table 10. This dual mechanism provides a physically consistent basis for the exceptional macroscopic strength improvements recorded in this study. It is important to acknowledge that this theoretical homogenization relies on assumed standard Poisson's ratios for the CP (0.20) and LS (0.25); however, a basic sensitivity analysis indicates that minor natural variations in these assumed constants (e.g., ±0.02) alter the final predicted composite modulus by less than 1.5%, thereby confirming the mathematical robustness of the 34.6 GPa theoretical prediction. Nevertheless, assuming homogeneous Poisson's ratios for a highly heterogeneous, sonicated, and DP-modified matrix remains a model simplification; future modelling should integrate experimentally derived dynamic Poisson's ratios via Ultrasonic pulse velocity (UPV) measurements.

4.4. Limits of validity and boundary conditions

The integrated multi-scale methodology substantially mitigates typical ITZ characterisation artefacts, though inherent uncertainties from section preparation, epoxy penetration depth, and indentation positioning must be acknowledged. Stereological overestimation of ITZ thickness arising from non-perpendicular sectioning angles was effectively eliminated through rigorous spatial calibration and morphological filtering of exclusively perpendicular aggregate-paste interfaces [29]; the reported 30–62% ITZ width reductions therefore reflect true spatial densification rather than geometric artefacts. The ~150 μm baseline ITZ width, while at the upper range of reported literature values, is physically justified by the specific combination of high w/b ratio, unactivated coarse DP particles, and reactive limestone aggregate present in the unsonicated reference specimens, and is visually corroborated by the broad fluorescence zone evident [23,25] in Fig. 9a. The precisely calibrated microindentation approach, operating at the micro-to-meso scale, avoids overlapping penetration errors, clinker anomalies, and roughness biases that frequently compromise nanoscale grid measurements [30,79]. It should additionally be noted that vacuum epoxy impregnation can artificially fill natural pores and distort local mechanical response [29,80]; the calibrated grid spacing and indent-to-boundary positioning protocol adopted here (±5 μm, Section 2.2) were specifically selected to minimise this artefact. Crucially, while vacuum epoxy impregnation inherently risks artificially increasing local stiffness in highly porous zones, the 27.4% differential increase in cement matrix hardness observed between the unsonicated and PUS-treated LS systems cannot be attributed to epoxy-induced artefacts. Because all compared specimens (both unsonicated controls and PUS-treated) underwent identical vacuum impregnation protocols, the systematic baseline error is normalized. The recorded mechanical enhancements, therefore, represent true physical-chemical matrix densification rather than variable resin intrusion.

SEM characterisation was deliberately performed at 7 d to preserve the early-age microstructural signature of PUS treatment; direct quantitative comparisons with the 28 d MIP and microindentation data should account for the ~40–45% additional strength gains occurring between these ages (Figs. 3 and 4), and future studies should incorporate 28 d SEM characterisation for full temporal completeness. The deliberate selection of a 7-day curing age for SEM characterization was critical to visually isolating the immediate physical mechanisms of PUS (acoustic defoaming, enhanced dispersion, and matrix consolidation) before they are completely obscured by massive late-age pozzolanic C-S-H deposition. However, the progressive pore refinement recorded by MIP at 28 d, coupled with the ultimate 55–60% f_c gains, confirms that the early microstructural framework established and captured by SEM at 7 days provides a permanent, stable foundation for the long-term chemical densification of the composite.

The primary scaling limitation concerns macroscopic geometry rather than measurement reliability. The model MC was designed with a deliberately reduced aggregate-to-cement ratio to isolate aggregate–paste contact zones, yielding a larger aggregate spacing factor than in commercial mixtures where reduced spacing promotes ITZ percolation [24,27]; full parametric validation of the Lu–Torquato and Mori–Tanaka frameworks for commercial aggregate gradations constitutes an essential direction for future multi-scale numerical studies [26,78]. Furthermore, as all ITZ and indentation measurements were performed exclusively on DP-modified specimens, strict decoupling of individual DP and PUS contributions was not achievable; the reported indentation changes therefore represent conservative lower bounds, corroborated by companion paste-level data demonstrating 27.2% and 19.5% increases in EM and Indentation hardness at 120 d [43].

4.5. Energy economics and scalability prospects

Real-time metering data [43] quantify the specific energy input precisely: a 10 min. PUS treatment of a single paste batch (0.675 kg) consumes 0.070 ± 0.003 kWh, scaling to approximately 78.8 kWh/m^3 at the experimental binder content (507 kg/m^3, w/b = 0.50). The

Table 10
Multi-scale performance summary: effect of 10 min PUS treatment in the LS system (MC_LS + DP vs. MC_LS + DP_10 min. PUS).

Key result	Model used	Before PUS	After PUS	Change
3D ITZ volume fraction (V_{ITZ})	Lu-Torquato	3.0%	1.1%	−63%
Composite elastic modulus (E_{hom})	Mori-Tanaka	32.2 GPa	34.6 GPa	+7.5%
CM hardness (near ITZ)	Microindentation	357.1 MPa	455.1 MPa	+27.4%
ITZ width (fluorescence microscopy)	2D image analysis	≈150 μm	37–91 μm (mean 57.4)	−62%
Compressive strength (28 d)	Experiment	28.4 MPa	44.1 MPa	+55%

embodied CO_2 saved through 20% cement replacement (~101 kg cement × 0.83 kg CO_2/kg ≈ 84 kg CO_2/m^3) corresponds to ~347 kWh eq. based on the 2023 EU average grid carbon intensity (0.242 kg CO_2/kWh [81]), yielding an energy-to-benefit ratio of ~23%. Proportional scaling to conventional commercial mixes (C25/30 per EN 206; 280–380 kg binder/m^3) reduces both the PUS demand (40-55 kWh/m^3) and the CO_2 savings (192-260 kWh eq.) proportionally, preserving the ~23% ratio and confirming that the net environmental balance remains strongly positive across practical mix designs. A full life-cycle assessment incorporating transducer efficiency, equipment amortization, and logistics is nonetheless required before definitive sustainability claims can be comprehensively quantified.

Contextualized against conventional SCM activation - which typically requires energy-intensive thermal calcination exceeding 1000 °C or prolonged mechanical grinding [43], the 10 min ambient-temperature PUS treatment represents a markedly more energy-efficient valorisation pathway for low-grade DP. Beyond energy considerations, PUS uniquely counteracts the high water demand inherent to porous diatomite particles, improving fresh mixture consistency without recourse to excessive chemical admixture dosages [43], a practical benefit with direct implications for mix design optimisation at an industrial scale. Critically, the energy invested in PUS does not merely offset the strength deficit associated with 20% cement replacement; it fundamentally upgrades the composite through selective macropore elimination and ITZ network disruption, yielding a high-performance material with 55–60% compressive strength gains.

5. Conclusions

This study presents a systematic multi-scale investigation of PUS-assisted interfacial engineering in a two-phase particulate composite system, demonstrating that acoustic activation of a diatomite supplementary cementitious phase produces synergistic microstructural improvements at the matrix–inclusion interface that translate directly to exceptional macroscopic composite performance. The following primary conclusions are drawn.

1. Combined DP + PUS treatment substantially improves macroscopic performance through complementary mechanisms. DP incorporation (20% cement replacement) combined with PUS treatment improved composite f_c by 55–60% and f_{fl} by 50–62% at 28 d, with total porosity reductions of 26–53%. DP primarily eliminated large macropore defects (>1000 nm), reducing their volume fraction from 5.22% to 0.26% (DI) and from 3.43% to 0.56% (LS), while PUS drove bulk matrix densification and chemical-physical hardening. This is consistent with a 12.8% increase in cumulative heat release (R^3 isothermal calorimetry at 40 °C), confirming a non-linear reactivity–sonication duration relationship (minimal gains at 5 min, +1.1%; substantial at 10 min, +12.8%; diminishing at 15 min, +3.0% marginal) that establishes R^3 calorimetry as a validated rapid screening tool for optimising PUS treatment parameters.
2. Aggregate mineralogy governs the magnitude of interfacial refinement, and macroscopic strength is decoupled from total porosity. In LS systems, DP + PUS increased CM hardness by 27.4% and EM by 10.3%, and reduced ITZ width by ~62% (from ~150 μm to 57.4 ± 15.1 μm) through synergistic chemical-physical bonding; in DI systems, improvements were modest (hardness +1.6%, modulus +3.1%, ITZ width −30%, from ~144 μm to 100.6 ± 26.8 μm), governed exclusively by physical consolidation. Direct evidence resolves the apparent "porosity paradox": the best-performing mixture (MC_LS + DP_10 min. PUS, f_c = 44.1 MPa) showed higher total porosity (11.24%) than its unsonicated counterpart (8.89%), demonstrating that macroscopic strength is governed by selective elimination of Griffith-type macropores and ITZ width reduction rather than bulk porosity alone.
3. Analytical upscaling mathematically links nanoscale interfacial healing to macroscopic stiffness gains. Lu–Torquato spatial modelling showed that PUS-induced ITZ narrowing in LS systems reduced the 3D ITZ volume fraction from 3.0% to 1.1% (−63%), approaching the estimated percolation threshold (~1–2% for V_{agg} = 0.568) and substantially disrupting the interconnected weak network. Consistently, Mori–Tanaka micromechanical homogenization predicted a 7.5% increase in composite EM (32.2 → 34.6 GPa), driven by simultaneous ITZ volume-fraction reduction and CM stiffening (21.3 → 23.5 GPa), validating the coherence of the multi-scale analytical framework.
4. The process offers an energy-efficient and industrially scalable pathway for sustainable composite production. Energy-balance analysis confirmed a strongly positive sustainability outcome: the PUS electrical energy cost scaled to 1 m^3 (~78.8 kWh) represents only ~23% of the CO_2 savings equivalent (~347 kWh eq.) achieved through 20% cement replacement. The identified 10 min. PUS threshold upgrades locally available, low-grade diatomite (SiO_2 ≈ 70%) into a highly reactive SCM without energy-intensive calcination or prolonged mechanical grinding, providing practical parameters for upscaling studies and industrial evaluation.

These findings advance fundamental understanding of PUS-cement interactions while providing practical guidance for developing sustainable, high-performance particulate composites with enhanced interfacial properties through cost-effective physical processing methods.

CRediT authorship contribution statement

Paweł Lisowski: Writing – review & editing, Writing – original draft, Visualization, Validation, Methodology, Investigation, Formal analysis, Data curation, Conceptualization. **Daria Jóźwiak-Niedźwiedzka:** Investigation. **Kamil Bochenek:** Investigation. **Michał A. Glinicki:** Writing – review & editing, Supervision, Conceptualization.

Declaration of competing interest

The authors declare that they have no known competing financial interests or personal relationships that could have appeared to influence the work reported in this paper.

Data availability

Data will be made available on request.

References

[1] Scrivener KL, Crumbie AK, Laugesen P. The interfacial transition zone (ITZ) between cement paste and aggregate in concrete. Interface Sci 2004;12:411–21. https://doi.org/10.1023/B:INTS.0000042339.92990.4c.
[2] Gao Y, Hu C, Zhang Y, Li Z, Pan J. Characterisation of the interfacial transition zone in mortars by nanoindentation and scanning electron microscope. Mag Concr Res 2018;70:965–72. https://doi.org/10.1680/jmacr.17.00161.
[3] He J, Lei D, Xu W. In-situ measurement of nominal compressive elastic modulus of interfacial transition zone in concrete by SEM-DIC coupled method. Cem Concr Compos 2020;114:103779. https://doi.org/10.1016/j.cemconcomp.2020.103779.
[4] Wong HS, Zobel M, Buenfeld NR, Zimmerman RW. Influence of the interfacial transition zone and microcracking on the diffusivity, permeability and sorptivity of cement-based materials after drying. Mag Concr Res 2009;61:571–89. https://doi.org/10.1680/macr.2008.61.8.571.
[5] Vargas P, Restrepo-Baena O, Tobón JI. Microstructural analysis of interfacial transition zone (ITZ) and its impact on the compressive strength of lightweight concretes. Constr Build Mater 2017;137:381–9. https://doi.org/10.1016/j.conbuildmat.2017.01.101.
[6] Liao KY, Chang PK, Peng YN, Yang CC. A study on characteristics of interfacial transition zone in concrete. Cem Concr Res 2004;34:977–89. https://doi.org/10.1016/j.cemconres.2003.11.019.
[7] Wu K, Shi H, Xu L, Ye G, De Schutter G. Microstructural characterization of ITZ in blended cement concretes and its relation to transport properties. Cem Concr Res 2016;79:243–56. https://doi.org/10.1016/j.cemconres.2015.09.018.
[8] Sicat E, Gong F, Ueda T, Zhang D. Experimental investigation of the deformational behavior of the interfacial transition zone (ITZ) in concrete during freezing and

thawing cycles. Constr Build Mater 2014;65:122–31. https://doi.org/10.1016/j.conbuildmat.2014.04.035.
[9] Nitka M, Tejchman J. Meso-mechanical modelling of damage in concrete using discrete element method with porous ITZs of defined width around aggregates. Eng Fract Mech 2020;231:107029. https://doi.org/10.1016/j.engfracmech.2020.107029.
[10] Lyu K, Garboczi EJ, She W, Miao C. The effect of rough vs. smooth aggregate surfaces on the characteristics of the interfacial transition zone. Cem Concr Compos 2019;99:49–61. https://doi.org/10.1016/j.cemconcomp.2019.03.001.
[11] Gao X, Liu QF, Cai Y, Tong LY, Peng Z, Xiong QX, De Schutter G. A new model for investigating the formation of interfacial transition zone in cement-based materials. Cem Concr Res 2025;187:107675. https://doi.org/10.1016/j.cemconres.2024.107675.
[12] Gao Y, De Schutter G, Ye G, Huang H, Tan Z, Wu K. Characterization of ITZ in ternary blended cementitious composites: experiment and simulation. Constr Build Mater 2013;41:742–50. https://doi.org/10.1016/j.conbuildmat.2012.12.051.
[13] Tasong WA, Lynsdale CJ, Cripps JC. Aggregate-cement paste interface: part I. Influence of aggregate geochemistry. Cem Concr Res 1999;29:1019–25. https://doi.org/10.1016/S0008-8846(99)00086-1.
[14] Zhang M, Gjørv OE. Microstructure of the interfacial zone between lightweight aggregate and cement paste. Cem Concr Res 1990;20:610–8. https://doi.org/10.1016/0008-8846(90)90103-5.
[15] Mindess S, Young JF, Darwin D. Concrete. second ed. Upper Saddle River, NJ: Prentice Hall; 2003.
[16] Alexander M, Mindess S. Aggregates in concrete. London: Taylor & Francis; 2005. https://doi.org/10.1201/9781482264647.
[17] Xiao J, Li W, Corr DJ, Shah SP. Effects of interfacial transition zones on the stress–strain behavior of modeled recycled aggregate concrete. Cem Concr Res 2013;52:82–99. https://doi.org/10.1016/j.cemconres.2013.05.004.
[18] Im S, Liu J, Cho S, Moon J, Park J, Wi K, Seok S, Lim S, Bae S. Quantitative characterization of the interfacial transition zone around lightweight and normal aggregates in cement mortars at different water-to-binder ratios. Constr Build Mater 2023;400:132584. https://doi.org/10.1016/j.conbuildmat.2023.132584.
[19] Bonavetti V, Donza H, Rahhal V, Irassar E. Influence of initial curing on the properties of concrete containing limestone blended cement. Cem Concr Res 2000;33:703–8. https://doi.org/10.1016/S0008-8846(00)00217-9.
[20] Scrivener KL, Nemati KM. The percolation of pore space in the cement paste/aggregate interfacial zone of concrete. Cem Concr Res 1996;26:35–40. https://doi.org/10.1016/0008-8846(95)00185-9.
[21] Bentz DP, Garboczi EJ, Lagergren ES. Multi-scale microstructural modeling of concrete diffusivity: identification of significant varibles. Cem Concr Aggregates 1998;20:129–39. https://doi.org/10.1520/CCA10446J.
[22] Gao Y, De Schutter G, Ye G, Tan Z, Wu K. The ITZ microstructure, thickness and porosity in blended cementitious composite: effects of curing age, water to binder ratio and aggregate content. Composites, Part B Eng 2014;60:1–13. https://doi.org/10.1016/j.compositesb.2013.12.021.
[23] Diamond S, Huang J. The ITZ in concrete – a different view based on image analysis and SEM observations. Cem Concr Compos 2001;23:179–88. https://doi.org/10.1016/S0958-9465(00)00065-2.
[24] Gao Y, De Schutter G, Ye G. Micro- and meso-scale pore structure in mortar in relation to aggregate content. Cem Concr Res 2013;52:149–60. https://doi.org/10.1016/j.cemconres.2013.05.011.
[25] Elsharief A, Cohen MD, Olek J. Influence of aggregate size, water cement ratio and age on the microstructure of the interfacial transition zone. Cem Concr Res 2003;33:1837–49. https://doi.org/10.1016/S0008-8846(03)00205-9.
[26] Lyu K, She W, Chang H, Gu Y. Effect of fine aggregate size on the overlapping of interfacial transition zone (ITZ) in mortars. Constr Build Mater 2020;248:118559. https://doi.org/10.1016/j.conbuildmat.2020.118559.
[27] Chung S-Y, Kim J-S. Investigation of gradient properties for cement mortar interfacial transition zones and their effects on mechanical characteristics using micro-CT. Dev Built Environ 2024;18:100390. https://doi.org/10.1016/j.dibe.2024.100390.
[28] Ji X, Chen Y, Hou Y, Dai C, Chen B, Zou H. Surface microscopic properties of various aggregates using laser scanning confocal microscope. Constr Build Mater 2021;290:123222. https://doi.org/10.1016/j.conbuildmat.2021.123222.
[29] Head MK, Wong HS, Buenfeld NR. Characterising aggregate surface geometry in thin-sections of mortar and concrete. Cem Concr Res 2008;38:1227–31. https://doi.org/10.1016/j.cemconres.2008.04.004.
[30] Sorelli L, Constantinides G, Ulm F-J, Toutlemonde F. The nano-mechanical signature of ultra high performance concrete by statistical nanoindentation techniques. Cem Concr Res 2008;38:1447–56. https://doi.org/10.1016/j.cemconres.2008.09.002.
[31] Grondin F, Matallah M. How to consider the interfacial transition zones in the finite element modelling of concrete? Cem Concr Res 2014;58:67–75. https://doi.org/10.1016/j.cemconres.2014.01.009.
[32] Wang Y, Zhang W, Lou G, Yao T. Effect of limestone powder on mechanical properties of concrete based on Griffith's microcracking theory. Constr Build Mater 2024;449:138413. https://doi.org/10.1016/j.conbuildmat.2024.138413.
[33] Wang Y, Zhang W, Wang J, Huang R, Lou G, Luo S. Effects of coarse aggregate size on thickness and micro-properties of ITZ and the mechanical properties of concrete. Cem Concr Compos 2024;154:105777. https://doi.org/10.1016/j.cemconcomp.2024.105777.
[34] Yao T, Wang Y, Li M, Zhang W, Luo S, Tian Q, Chen J. Recycling coal gasification slag to produce eco-friendly ultra-high performance concrete: working properties, mechanical properties and microstructure. Cem Concr Compos 2025;164:106260. https://doi.org/10.1016/j.cemconcomp.2025.106260.
[35] Ganjian E, Ehsani A, Mason TJ, Tyrer M. Application of power ultrasound to cementitious materials: advances, issues and perspectives. Mater Des 2018;160:503–13. https://doi.org/10.1016/j.matdes.2018.09.043.
[36] Lisowski P, Jozwiak-Niedzwiedzka D, Osial M, Bochenek K, Denis P, Glinicki MA. Power ultrasound-assisted enhancement of granulated blast furnace slag reactivity in cement paste. Cem Concr Compos 2024;154:105781. https://doi.org/10.1016/j.cemconcomp.2024.105781.
[37] Xiong G, Fang Z, Ren Y, Jia X, Luo H, Yang J, Ran B, Zhou S, Wang C. A novel defoaming technology for cement paste by using power ultrasound treatment. Cem Concr Res 2026;200:108072. https://doi.org/10.1016/j.cemconres.2025.108072.
[38] Remus R, Roßler C, Peters S, Sowoidnich T, Ludwig H-M. Fundamental effects of using power ultrasound to accelerate C_3S hydration. Cem Concr Res 2024;180:107514. https://doi.org/10.1016/j.cemconres.2024.107514.
[39] Chen Y, Hou Y, Ji X, Zou H, Dai C, Chen B. Characterization of surface mechanical properties of various aggregates from micro scale using AFM. Constr Build Mater 2021;286:122847. https://doi.org/10.1016/j.conbuildmat.2021.122847.
[40] Duan S, Cui J, Hu J, Han T, Chen Y, Wang H, Ma T. Research on the adhesion mechanism and compatibility of acrylate composite polyurethane binder – aggregate based on surface free energy theory. Constr Build Mater 2024;438:137236. https://doi.org/10.1016/j.conbuildmat.2024.137236.
[41] Hassan HMZ, Wu K, Huang W, Chen S, Zhang Q, Xie J, Cai X. Study on the influence of aggregate strength and shape on the performance of asphalt mixture. Constr Build Mater 2021;294:123599. https://doi.org/10.1016/j.conbuildmat.2021.123599.
[42] Hu J, Huang Q, Lou N, Luo S. Microstructural characteristics of interfacial zone in asphalt mixture considering the influence of aggregates properties. Materials 2020;13:2558. https://doi.org/10.3390/ma13112558.
[43] Lisowski P, Bochenek K, Osial M, Denis P, Gawlicki M, Glinicki MA. Power ultrasound treatment for a sustainable production of diatomite-containing cement-based materials. J Build Eng 2026;118:114989. https://doi.org/10.1016/j.jobe.2025.114989.
[44] Sun M, Zou C, Xin D. Pore structure evolution mechanism of cement mortar containing diatomite subjected to freeze-thaw cycles by multifractal analysis. Cem Concr Compos 2020;114:103731. https://doi.org/10.1016/j.cemconcomp.2020.103731.
[45] Akhtar F, Rehman Y, Bergström L. A study of the sintering of diatomaceous earth to produce porous ceramic monoliths with bimodal porosity and high strength. Powder Technol 2010;201:253–7. https://doi.org/10.1016/j.powtec.2010.04.004.
[46] Zhang G, Cai D, Wang M, Zhang C, Zhang J, Wu Z. Microstructural modification of diatomite by acid treatment, high-speed shear, and ultrasound. Microporous Mesoporous Mater 2013;165:106–12. https://doi.org/10.1016/j.micromeso.2012.08.005.
[47] Lorwanishpaisarn N, Kasemsiri P, Posi P, Chindaprasirt P. Characterization of paraffin/ultrasonic-treated diatomite for use as phase change material in thermal energy storage of buildings. J Therm Anal Calorim 2017;128:1293–303. https://doi.org/10.1007/s10973-016-6024-3.
[48] Hassan HS, Shi C, Hashem FS, Israde-Alcantara I, Pfeiffer H. Exploring diatomite as a novel natural resource for ecofriendly-sustainable hybrid cements. Resour Conserv Recycl 2024;202:107402. https://doi.org/10.1016/j.resconrec.2023.107402.
[49] Ferreira RLS, Pinto L, Nóbrega AF, Carneiro AMP. Diatomaceous earth: a review of its characteristics and effects on the properties of mortars. Constr Build Mater 2024;421:135711. https://doi.org/10.1016/j.conbuildmat.2024.135711.
[50] Liao S, Xu H, Wu L, Zhao Z, Ma K. Strength formation mechanism and microstructural evolution of low-grade diatomite-based cementitious materials. Constr Build Mater 2024;431:136588. https://doi.org/10.1016/j.conbuildmat.2024.136588.
[51] Londono-Zuluaga D, Gholizadeh-Vayghan A, Winnefeld F, Avet F, Ben Haha M, Bernal S, Cizer Ö, Cyr M, Dolenec S, Durdzinski P, Haufe J, Hooton D, Kamali-Bernard S, Li X, Marsh ATM, Marroccoli M, Mrak M, Muy Y, Patapy C, Pedersen M, Sabio S, Schulze S, Snellings R, Telesca A, Vollpracht A, Ye G, Zhang S, Scrivener KL. Report of RILEM TC 267-TRM Phase 3: validation of the R^3 reactivity test. Mater Struct 2022;55:142. https://doi.org/10.1617/s11527-022-01947-3.
[52] Koufany I, De la Torre AG, Redondo-Soto C, Santacruz I, Cuesta A, Gastaldi D, Canonico F, Mazanec O, Aranda MAG. General correlation between R^3 test results and compressive strengths for five families of supplementary cementitious materials. Cem Concr Compos 2025;163:106166. https://doi.org/10.1016/j.cemconcomp.2025.106166.
[53] Williams SL, Beatty DN, Srubar III WV. A small-scale thermogravimetric method to measure the chemical reactivity of supplementary cementitious materials. Cement 2023;12:100071. https://doi.org/10.1016/j.cement.2023.100071.
[54] EN 196-12. Methods of testing cement - part 12: reactivity of cement constituents - heat of hydration and bound water content methods. 2024. 2024.
[55] ASTM C1897-20. Standard test methods for measuring the reactivity of supplementary cementitious materials by isothermal calorimetry and bound water measurements. West Conshohocken, PA: ASTM International; 2020. https://doi.org/10.1520/C1897-20.
[56] Snellings R, Suraneni P, Skibsted J. Future and emerging supplementary cementitious materials. Cem Concr Res 2023;171:107199. https://doi.org/10.1016/j.cemconres.2023.107199.
[57] Avet F, Li X, Haha MB, Bernal SA, Bishnoi S, Cizer O, Cyr M, Dolenec S, Durdzinski P, Haufe J, Hooton D, Juenger MCG, Kamali-Bernard S, Londono-Zuluaga D, Marsh ATM, Marroccoli M, Mrak M, Parashar A, Patapy C, Pedersen M, Provis JL, Sabio S, Schulze S, Snellings R, Telesca A, Thomas M, Vargas F, Vollpracht A, Walkley B, Winnefeld F, Ye G, Zhang S, Scrivener K. Report of RILEM TC 267-TRM phase 2: optimization and testing of the robustness of the R^3 reactivity

tests for supplementary cementitious materials. Mater Struct 2022;55:92. https://doi.org/10.1617/s11527-022-01928-6.
[58] Frías M, Alujas A, Moreno-Reyes A, Ibanez JA, Paredes MV, Vegas I. Advances in understanding R^3 chemical reactivity in various traditional and emerging pozzolans: Chemical, mineralogical and calorimetric dimensions. Constr Build Mater 2024;457:139474. https://doi.org/10.1016/j.conbuildmat.2024.139474.
[59] Glinicki MA, Zielinski M. Depth-sensing indentation method for evaluation of effectiveness of secondary cementitious materials. Cem Concr Res 2004;34:721–4. https://doi.org/10.1016/j.cemconres.2003.10.014.
[60] Ranachowski Z, Glinicki MA, Nowowiejski G. Application of acoustic emission method for concrete component identification during microhardness testing. Cement-Wapno-Beton = Cement Lime Concrete 2010;15:202–9.
[61] ASTM C856/C856M-20. Standard practice for petrographic examination of hardened concrete. West Conshohocken, PA: ASTM International; 2020. https://doi.org/10.1520/C0856_C0856M-20.
[62] Jakobsen UH, Laugesen P, Thaulow N. Determination of water-cement ratio in hardened concrete by optical fluorescence microscopy, ACI SP-191. Farmington Hills, MI: American Concrete Institute; 1999. p. 27–42. https://doi.org/10.14359/5732.
[63] Glinicki MA, Litorowicz A. Crack system evaluation in concrete elements at mesoscale. Bull Pol Acad Sci Tech Sci 2006;54:371–9.
[64] Jozwiak-Niedzwiedzka D. Influence of blended cements on the concrete resistance to carbonation. In: Proc. Int. Symp. ,Brittle matrix composites 10. Woodhead Publishing; 2012. p. 125–34. https://doi.org/10.1533/9780857099891.125.
[65] Dąbrowski M, Jozwiak-Niedzwiedzka D, Bogusz K, Glinicki MA. Influence of serpentinite aggregate on the microstructure and durability of radiation shielding concrete. Constr Build Mater 2022;337:127536. https://doi.org/10.1016/j.conbuildmat.2022.127536.
[66] Yio MHN, Wong HS, Buenfeld NR. 3D pore structure and mass transport properties of blended cementitious materials. Cem Concr Res 2019;117:23–37. https://doi.org/10.1016/j.cemconres.2018.12.007.
[67] Lu B, Torquato S. Nearest-surface distribution functions for polydispersed particle systems. Phys Rev A 1992;45:5530–44. https://doi.org/10.1103/PhysRevA.45.5530.
[68] Diamond S. Mercury porosimetry: an inappropriate method for the measurement of pore size distributions in cement-based materials. Cem Concr Res 2000;30:1517–25. https://doi.org/10.1016/S0008-8846(00)00370-7.
[69] Chen Y, Al-Neshawy F, Punkki J. Investigation on the effect of entrained air on pore structure in hardened concrete using MIP. Constr Build Mater 2021;292:123441. https://doi.org/10.1016/j.conbuildmat.2021.123441.
[70] Wong HS, Poole AB, Wells B, Eden M, Barnes R, Ferrari J, Fox R, Yio MHN, Copuroglu O, Guðmundsson G, Hardie R, Jakobsen UH, Makoubi K, Mitchinson A, Raybould P, Strongman J, Buenfeld NR. Microscopy techniques for determining water–cement (w/c) ratio in hardened concrete: a round-robin assessment. Mater Struct 2020;53:25. https://doi.org/10.1617/s11527-020-1458-2.
[71] Jakobsen UH, Brown DR. Reproducibility of w/c ratio determination from fluorescent impregnated thin sections. Cem Concr Res 2006;36:1567–73. https://doi.org/10.1016/j.cemconres.2006.05.003.
[72] Chen Q, Zhang J, Wang Z, Zhao T, Wang Z. A review of the interfacial transition zones in concrete: identification, physical characteristics, and mechanical properties. Eng Fract Mech 2024;300:109979. https://doi.org/10.1016/j.engfracmech.2024.109979.
[73] Ioannou I, Fournari R, Petrou MF. Testing the soundness of aggregates using different methodologies. Constr Build Mater 2013;40:604–10. https://doi.org/10.1016/j.conbuildmat.2012.11.047.
[74] Khedmati M, Kim Y-R, Turner JA, Alanazi H, Nguyen C. An integrated microstructural-nanomechanical-chemical approach to examine material-specific characteristics of cementitious interphase regions. Mater Charact 2018;138:154–64. https://doi.org/10.1016/j.matchar.2018.01.045.
[75] Georget F, Wilson W, Scrivener KL. Edxia: microstructure characterisation from quantified SEM-EDS hypermaps. Cem Concr Res 2021;141:106327. https://doi.org/10.1016/j.cemconres.2020.106327.
[76] Garboczi EJ, Bentz DP. Analytical formulas for interfacial transition zone properties. Adv Cement Base Mater 1997;6:99–108. https://doi.org/10.1016/S1065-7355(97)90016-X.
[77] Jia Z, Han Y, Zhang Y, Qiu C, Hu C, Li Z. Quantitative characterization and elastic properties of interfacial transition zone around coarse aggregate in concrete. J Wuhan Univ Technol -Materials Sci Ed 2017;32:838–44. https://doi.org/10.1007/s11595-017-1677-8.
[78] Brown L, Allison PG, Sanchez F. Use of nanoindentation phase characterization and homogenization to estimate the elastic modulus of heterogeneously decalcified cement pastes. Mater Des 2018;142:308–18. https://doi.org/10.1016/j.matdes.2018.01.030.
[79] He J, Lei D, Di Luzio G, Zhu F, Bai P. Mechanical properties measurement and micro-damage characterization of ITZ in concrete by SEM-DIC method. Opt Laser Eng 2022;155:107064. https://doi.org/10.1016/j.optlaseng.2022.107064.
[80] Memon SA, Bekzhanova Z, Murzakarimova A. A review of improvement of interfacial transition zone and adherent mortar in recycled concrete aggregate. Buildings 2022;12:1600. https://doi.org/10.3390/buildings12101600.
[81] Ember, European Electricity Review 2024. Ember Energy 2024. Available at: https://ember-energy.org/latest-insights/european-electricity-review-2024/.